

國立中央大學

物理學系

碩士論文（初稿）

VUV and EUV irradiation of  $\text{CH}_4 + \text{NH}_3$   
ice mixtures

研究生: Leung Pui Shan

指導教授: Chen Yu Jung

中華民國一百零六年十二月

國立中央大學

物理學系

碩士論文（初稿）

VUV and EUV irradiation of  $\text{CH}_4 + \text{NH}_3$   
ice mixtures

研究生: Leung Pui Shan

指導教授: Chen Yu Jung

中華民國一百零六年十二月

版權所有© Leung Pui Shan 2017



## VUV and EUV irradiation of $\text{CH}_4 + \text{NH}_3$ ice mixtures

### 中文摘要

關鍵字：星際冰晶，冥衛一，真空紫外光，超真空紫外光

人類從未停止對外太空的探索。爲了尋找生命的起源，天文學家們觀測了一個又一個的星球。然而，除了觀測星球外，我們還能在實驗室模擬外太空的狀態，並把星際中的一些簡單份子製作出來。在實驗室模擬星際中的環境來達到探索生命起源的目的。在2002年，一群日本和美國科學家MIYAKAWA et al. (2002)[1]在被稀釋的放置在-78度的環境中27年的 $\text{NH}_4\text{CN}$ 中發現了鹼基(nucleobase)的一種(adenine)，而當中HCN正是胺基酸CN的來源。爲了探討 $\text{CN}^-$ 的生成，本文使用 $\text{CH}_4$ 和 $\text{NH}_3$ 在真空環境( $1 \times 10^{-10}$  torr)和非常低溫(15 K)的混合物，來模擬太陽系中的冥衛一(Charon)的表面。我們使用真空紫外光(VUV)和超真空紫外光(EUV)來模擬太陽系中的能量來源並使用傅里葉紅外光譜儀和四極質譜儀來探討 $\text{CN}^-$ 的生成。



## VUV and EUV irradiation of $\text{CH}_4 + \text{NH}_3$ ice mixtures

### 英文摘要

Keywords: interstellar ice, Charon, VUV irradiation, EUV irradiation

We never stop the exploration of the outer space. Since 1900s, astronomers have observed all over the sky to seek origin of life. Apart from observing stars, we may simulate the outer space environments and make some simple molecules in laboratories on the earth now. In 2002, a group of Japanese and US scientists (Miyakawa et al. (2002)[1]) used  $\text{NH}_4\text{CN}$ , which was placed in  $-78^\circ\text{C}$  for 27 years, discovered pyrimidine and purines. HCN is believed as the origin of nitrile group in amino acids. To investigate the formation of  $\text{CN}^-$ , we deposite  $\text{CH}_4$  and  $\text{NH}_3$  (mechanism proposed by Kim and Kaiser (2011)[2]) at 15 K and  $1 \times 10^{-10}$  torr to simulate the surface of Charon. We provide VUV and EUV irradiations as energy sources and mainly use Fourier Transform Infrared Spectrometer (FTIR) and Quadrupole Mass Spectroscopy (QMS) to study different concentrations of  $\text{CH}_4$  to  $\text{NH}_3$  ice mixtures.



## VUV and EUV irradiation of $\text{CH}_4 + \text{NH}_3$ ice mixtures

### 謝誌

在我的求學生涯中，有很多的老師。不過，讓我得益最多的還是這兩年多的碩士生涯。

還記得剛剛來台灣的時候，半個人都不認識，憑著老師一封電郵就來台灣唸書，實在是人生路不熟。這兩年裡面，最感謝的人就是我的指導教授，陳俞融老師。雖然老師對我並沒有好臉色，每次我報告完總是一副“奇怪，你怎麼又離題了”的樣子；但是我知道責之深愛之切，每次打開老師的面書，就會知道：喔，這次老師又要生我的氣了。

在整個碩士生涯中，我學會最多的就是如何篩選一篇相關的文獻，怎樣和我自己的論文相比較，從而得出究竟這篇文獻是否適用的過程。從一開始不會把整篇文獻看完，到後來認真地仔細地看別人引用的文章，再到後來自己寫出來的時候該如何引用。或者我的論文內容並不充實，但我認為碩士課程需要學習的就是如何有辨別文獻的相關性。並不是以偏概全，嘩眾取寵，而是只把自己有把握的地方撰寫出來。

本論文得以完成，實在是一件非常不容易的事情。由於本人英文寫作不佳，所以感謝好友Jess幫忙修改英文句子。謝謝學長samuel教我使用Latex，謝謝實驗室的學長豆花教導我做實驗，學弟妹謝妮恩，蘇映全，在同步輻射期間的幫忙。Thanks Angela, Guillermo and Michel for your valuable comments on my thesis, which actually helps. Finally, thanks molview.org for providing an open source tool to create 3D chemical models conveniently to make 3D diagrams.



# Contents

中文摘要 .....	i
	<b>page</b>
英文摘要 .....	ii
謝誌 .....	iii
Contents .....	iv
List of Figures .....	vi
List of Tables .....	ix
1. Introduction .....	1
2. Methods .....	6
2.1 Laboratory Astrophysics . . . . .	6
2.1.1 Experimental simulations by IPS system . . . . .	6
2.1.2 Vacuum-UV source . . . . .	9
2.1.3 Extreme EUV source . . . . .	11
2.2 Experimental Protocol . . . . .	11
2.2.1 Preparation of experiments and cooling . . . . .	11
2.2.2 Deposition . . . . .	12
2.2.3 Photon Irradiation . . . . .	12
2.2.4 Warmup . . . . .	12
2.3 Infra-red spectroscopy and the Beer-Lambert's Law .	13
2.4 Reaction Rate Laws . . . . .	15
3. Results and Discussions .....	17
3.1 The infrared spectra and peaks identification . . . . .	17
3.2 Reaction mechanisms and fitting results . . . . .	22
3.2.1 C <sub>2</sub> H <sub>6</sub> . . . . .	22
3.2.2 C <sub>3</sub> H <sub>8</sub> . . . . .	22
3.2.3 CN <sup>-</sup> . . . . .	23



3.3	The Concentration Effects in $\text{CN}^-$ formation and the relation with $\text{C}_2\text{H}_6$ and $\text{C}_3\text{H}_8$ . . . . .	26
3.3.1	Cyanide ion and Ethane . . . . .	26
3.4	Photon Energy Effect - EUV and VUV . . . . .	28
3.5	Residues . . . . .	34
3.6	Summary . . . . .	35
4.	Astrophysical Implications.....	36
4.1	The destruction of methane and ammonia by photon sources and electrons . . . . .	36
4.2	Cyanide ion produced by photon sources and electrons	37
4.3	Conclusion . . . . .	39



# List of Figures

Figure 1.1 The $2.2\mu\text{m}$ absorption taken by LEISA camera colored as green on the topology shown by LORRI camera (A) and the spectra at 4 positions (B) with b taken near organa crater.(quoted from [3]) . . . . .	3
Figure 1.2 The temperature of Charon with thermal inertia $10 \text{ J m}^{-2} \text{ K}^{-1} \text{ s}^{-1/2}$ in 1750 to 2050 Earth years (a) and longest time the Latitude is under 25 K with the model averaged for 3 Myr with 2.5 (solid) 10 (dotted) and 40 (dashed) $\text{J m}^{-2} \text{ K}^{-1} \text{ s}^{-1/2}$ (b).(quoted from [4]) . . . . .	4
Figure 2.1 The schematic diagram of IPS system, mechanical pumps are not shown for clarity. (Quoted from Chen et al. 2014) . . . . .	7
Figure 2.2 The cross-section of MDHL (T-type geometry) (Quoted from Chen et al. 2014). . . . .	9
Figure 2.3 VUV spectra of MDHL (T-type geometry, 110-180 nm) with different $\text{H}_2$ pressure inside the lamp(Quoted from Chen et al. (2014)[5]) . . . . .	10
Figure 2.4 Different vibrational modes of a three atom molecule. 14	
Figure 3.1 The the infrared spectrum of $\text{CH}_4 + \text{NH}_3$ ice mixtures before irradiation (black) and after VUV (MDHL) irradiated (coloured) ice mixtures. . . . .	18
Figure 3.2 The infrared spectra of $\text{CH}_4 + \text{NH}_3$ ice mixtures in the range of $\text{C}_2\text{H}_6$ and $\text{C}_3\text{H}_8$ vibrations before irradiation (black) and VUV irradiated ice mixtures provided by MDHL. . . . .	20





Figure 3.3	The infrared spectrum of $\text{CH}_4 + \text{NH}_3$ ice mixtures of $\text{C}_2\text{H}_6$ and $\text{C}_3\text{H}_8$ before irradiation (black) and VUV irradiated ice mixtures provided by MDHL. . . . .	21
Figure 3.4	The column density of $\text{C}_2\text{H}_6$ during $\text{CH}_4 + \text{NH}_3$ ice mixtures irradiated by MDHL. . . . .	23
Figure 3.5	The column density of $\text{C}_3\text{H}_8$ during $\text{CH}_4 + \text{NH}_3$ ice mixtures irradiated by MDHL. . . . .	24
Figure 3.6	The ion current with mass to charge ratio 31 detected by QMS during warm-up with heating rate 1 K/min in different relative proportions of ice mixtures. . .	25
Figure 3.7	The column density of $\text{CN}^-$ accumulated when different relative proportions of $\text{CH}_4 + \text{NH}_3$ ice mixtures are irradiated by VUV photons provided by MDHL. The dotted lines are fits of column densities by equation 2.10. .	26
Figure 3.8	The $\text{NH}_3$ in excess situation where increasing $\text{CH}_4$ concentrations enhances the production of $\text{CN}^-$ . The blue balls indicates N atoms, white balls indicates H atoms while grey ball is C atom. . . . .	27
Figure 3.9	The $\text{CH}_4$ in excess situation where $\text{CH}_4$ reacts with neighbouring $\text{CH}_4$ molecules producing $\text{C}_2\text{H}_6$ and $\text{C}_3\text{H}_8$ . The blue balls indicates N atoms, white balls indicates H atoms while grey balls are C atoms. . . . .	28
Figure 3.10	The column density of $\text{CN}^-$ and $\text{C}_2\text{H}_6$ accumulated when different relative proportions of $\text{CH}_4 + \text{NH}_3$ ice mixtures are irradiated by VUV photons provided by MDHL. . . . .	29
Figure 3.11	The the infrared spectrum of $\text{CH}_4 + \text{NH}_3$ ice mixtures before irradiation (black) and VUV and EUV (coloured) irradiated ice mixtures provided by MDHL. (a) and (b) are EUV irradiated $\text{CH}_4:\text{NH}_3 = 1:5$ and $3:2$ ice mixtures respectively, and (c) and (d) are VUV irradiated $\text{CH}_4:\text{NH}_3 = 1:5$ and $3:2$ ice mixtures respectively. . . . .	30



Figure 3.12 The column density of $C_3H_8$ divided by $C_2H_6$ accumulated when different relative proportions of $CH_4 + NH_3$ ice mixtures are irradiated by VUV and EUV photons	31
Figure 3.13 The normalized destruction of $CH_4$ and $NH_3$ in $CH_4 + NH_3$ ice mixtures irradiated by VUV and EUV photons . . . . .	32
Figure 3.14 The column densities of $CN^-$ generated by irradiation of $CH_4+NH_3$ ice mixtures by MDHL and 30.4 nm monochromatic light. . . . .	33
Figure 3.15 The IR spectrum of residues in after $CH_4:NH_3 = 3:2$ experiments and the accumulate residues after MDHL experiments and NSRRC experiments. . . . .	35
Figure 4.1 The calculated percentage of VUV irradiation absorbed by different thickness of $CH_4$ to $NH_3 = 3:2$ ice mixtures. . . . .	37



## List of Tables

Table 3.1	The strength of absorbance adopted in this thesis measured in literatures of pure ice samples . . . . .	17
Table 3.2	The peak positions of identified substances after irradiation in different relative proportions of ice mixtures.	21
Table 3.3	The fitting results of $C_2H_6$ by $[C_2H_6]=[C_2H_6]_o(1 - e^{-kt})$ . . . . .	22
Table 3.4	The fitting results of $C_3H_8$ by $[C_3H_8]=[C_3H_8](1 - e^{-k_1t})$	23
Table 3.5	The fitting results of $CN^-$ by equation 2.10 . . . . .	27
Table 3.6	The peak positions of identified substances after VUV and EUV irradiations in different relative propor- tions of ice mixtures. . . . .	31
Table 3.7	The fitting results of $CN^-$ by equation 2.10 . . . . .	33
Table 3.8	The peak positions of residues and their assignments	34



# 1. Introduction

According to Hindu cosmological mythology, ancient people believe that a giant turtle bears the world on its back. Even after we stepped onto the moon at 1969, there are still plenty that we cannot explain. Recently, a group of scientists put a dilute  $\text{NH}_4\text{CN}$  in temperature of liquid nitrogen for 27 years and discovered a wide variety of pyrimidine and purines [1].  $\text{NH}_4^+\text{CN}^-$  plays an important role in life evolution. The formation of  $\text{CN}^-$  is proposed by Kim and Kaiser (2001) [2], which is produced by ammonia ( $\text{NH}_3$ ) and methane ( $\text{CH}_4$ ). However, they have only demonstrated the effects of energetic electrons onto the ice mixtures, the photolysis experiments of  $\text{CH}_4+\text{NH}_3$  ice mixtures especially varying relative proportions of  $\text{CH}_4$  to  $\text{NH}_3$  by VUV or EUV photons has not been performed. This thesis aims to investigate the chemistry of VUV and EUV irradiations on  $\text{CH}_4+\text{NH}_3$  ice mixtures, which is possibly one of the main starting components to form  $\text{CN}^-$  in astrophysical environments.

$\text{NH}_3$  is often not probed in astrophysical environments unless detecting ambiguously because nearly all the infrared bands overlap with water. The "umbrella" mode ( $1070\text{ cm}^{-1}$ ) is often obscured by the 10 micron silicate feature [6]. It is often detected as ammonia hydrates ( $\text{NH}_3 \cdot n\text{H}_2\text{O}$ ) [7]. The New Horizons team has revealed a high concentration crater of  $\text{NH}_3$  on Charon [3]. Figure 1.1 presents the infrared spectra detected by LEISA camera regarding four different segments at the right panel. On Organa crater, we may observe a  $2.2\text{ }\mu\text{m}$  absorption representing presence of ammonia at "b" spectrum. The part b spectrum is enlarged at left bottom panel with the green pigments indicates the concentration of ammonia overlapped on topological graph of Charon. This also explains the different concentration of ammonia detected by



different earth-based observation groups cook et al (2007)[7] and brown et al. (2000)[8].

Charon, as a member in the Pluto system, is the second massive member with masses about half of Pluto. It orbits around Pluto, where Pluto is orbiting the Sun with an semi-major axis of 39.1 A.U. and period of 248 earth years. Similar to the earth and moon system, they orbits synchronized to each other with tidal-lockings, which the same side always facing each other.  $\text{CH}_4$  is the main ejecta arrived from Pluto to Charon (98 % by calculation of Hoey et al. (2017)[9]. According to the New Horizons team,  $\text{CH}_4$  from Pluto may accumulate onto the surface of Charon by cold-trapping which deposits at temperature below 25 K (at pressure  $7.4 \times 10^{-14}$  torr) onto the surface of Charon[4]. The amount of  $\text{CH}_4$  varies along the surface of Charon because it depends on the length of time the temperature is below 25 K which in turns depends on diurnal motion and thermal inertia of Charon. With obliquity of 119 degrees (currently) from the ecliptic, a long continuous darkness is expected. The upper panel of Figure 1.2 is the model simulated by Grundy et al. (2016)[4] presenting the surface temperature of Charon with respect to the latitude and time in earth years. Based on length of time the surface temperature falls below 25 K, he plotted the length of time that  $\text{CH}_4$  can accumulate onto Charon at the lower panel. From bottom panel, the mean cold-trap longitivity for depositing  $\text{CH}_4$  is 2 times longer at the poles (130 earth years) than at  $45^\circ$  latitude [4]. The non-detection of methane by infrared spectra implies that its concentration is less than ammonia. However, the exact concentration ratios to ammonia was not fully modelled yet. Therefore, we decided to perform 3 relative ratios of  $\text{CH}_4$  to  $\text{NH}_3$  (in excess) to simulate the surface of Charon. They includes  $\text{CH}_4$  to  $\text{NH}_3$  equals 1:5, 1:10 and 1:20.

Despite methane and ammonia, we still need energy to generate  $\text{CN}^-$ . In our solar system, there are many energetic sources, including solar wind, photons, cosmic rays from the outer solar system, etc. Among these, Ly- $\alpha$  photons appears to be the most important source

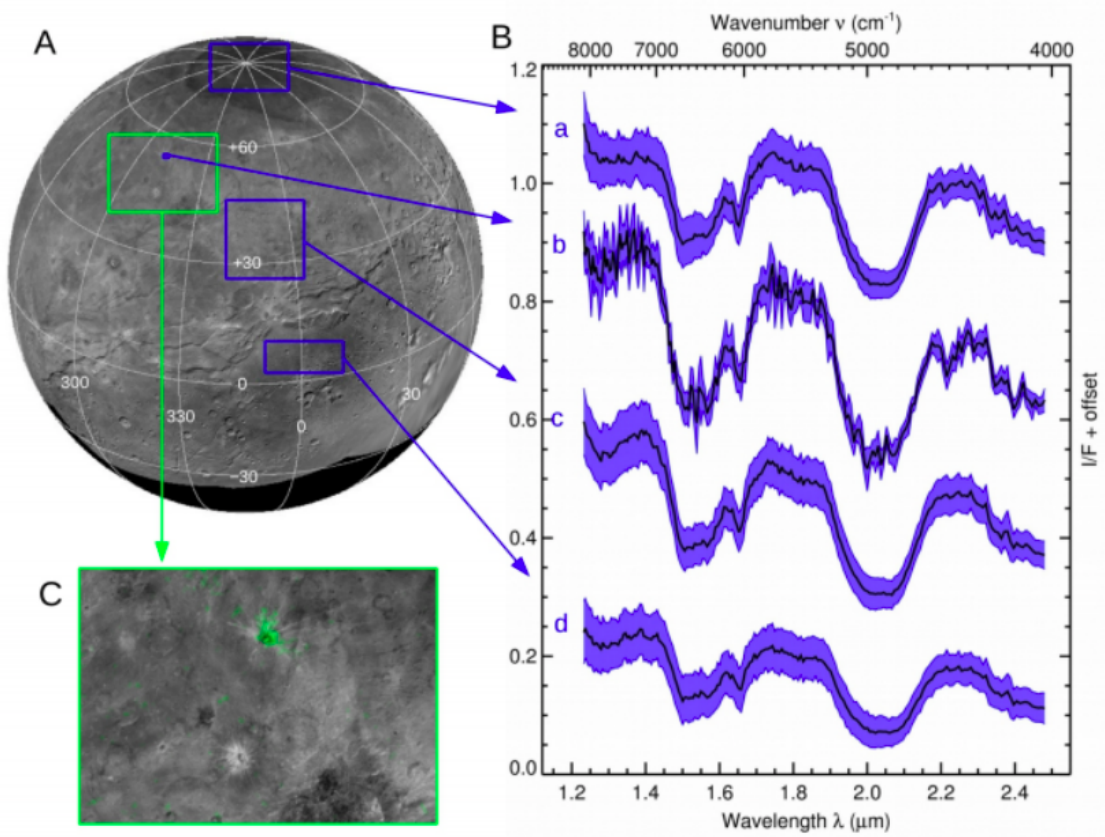


Figure 1.1: The  $2.2\mu\text{m}$  absorption taken by LEISA camera colored as green on the topology shown by LORRI camera (A) and the spectra at 4 positions (B) with b taken near Organa crater. (quoted from [3])

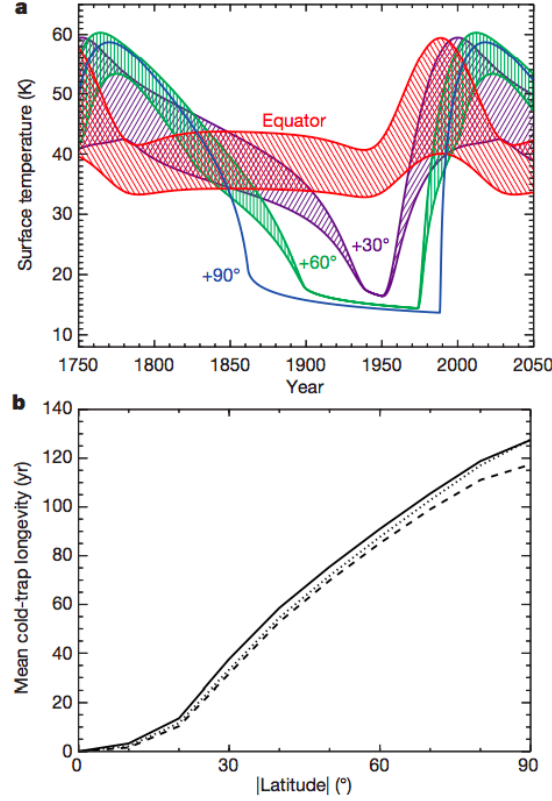


Figure 1.2: The temperature of Charon with thermal inertia  $10 \text{ J m}^{-2} \text{ K}^{-1} \text{ s}^{-1/2}$  in 1750 to 2050 Earth years (a) and longest time the Latitude is under 25 K with the model averaged for 3 Myr with 2.5 (solid) 10 (dotted) and 40 (dashed)  $\text{J m}^{-2} \text{ K}^{-1} \text{ s}^{-1/2}$  (b). (quoted from [4])

in the dark side of Charon. It is attributed from sunlit (70 %) and resonance scattering by atomic hydrogen flow (the excitation of electrons by hydrogen atoms and release Ly- $\alpha$  photons in all directions) (30 %) in the solar system [4]. Its flux is  $3.5 \times 10^7 \text{ photons cm}^{-2} \text{ s}^{-1}$  at the winter pole of Charon [4] which is 50 % larger than expected before Mission New Horizons [10]. We perform VUV irradiation on  $\text{CH}_4 + \text{NH}_3$  experiments with different ratios (including 3:2, 1:5, 1:10 and 1:20) to simulate the photon induced evolution on different concentrations of  $\text{CH}_4$ . The ratios in previous studies with electron irradiation experiments are  $\text{CH}_4$  to  $\text{NH}_3$  equals 3:1 [2] and 3:2 [11]. As a complete study, we decided performing a ratio of  $\text{CH}_4$  to  $\text{NH}_3$  equals 3:2 to make possible comparisons.

Apart from VUV irradiation, EUV irradiation also irradiates on Charon. The direct EUV irradiation ( $>12.4 \text{ eV}$ ) is  $8.7 \times 10^7 \text{ eV cm}^{-2} \text{ s}^{-1}$  at mean heliocentric distance 39 A.U. whereas VUV irradiation (Ly- $\alpha$  photons) is  $1.9 \times 10^9 \text{ eV cm}^{-2} \text{ s}^{-1}$  calculated by Grundy et al. (2016) [4].



In order to investigate the effectiveness of EUV to VUV irradiation, we keep temperature of  $\text{CH}_4 + \text{NH}_3$  (3:2 & 1:5) ice mixtures at 15 K and use the monochromatic 30.4 nm (40.8 eV) ,He II light provided by High flux beamline at National Synchrotron Radiation Research Centre (NSRRC) in Taiwan to irradiate the ice mixtures. The relative ratios of EUV irradiated ice is  $\text{CH}_4$  to  $\text{NH}_3 = 3:2$  and 1:5 for possible comparisons with VUV irradiations.

In this text, we will introduce the experimental methodology in chapter 2, the formation mechanisms of main products of EUV and VUV irradiated  $\text{CH}_4 + \text{NH}_3$  ice mixtures in chapter 3. With these results, we will know more details of Charon, especially the influences of photon sources. Different energy sources including electron irradiation experiments , EUV and VUV irradiations, and their astrophysical implications will be presented in chapter 4.





## 2. Methods

### 2.1 Laboratory Astrophysics

To study the chemical reactivities in astrophysical environments (surface of Charon during winter time) experimentally, we conduct our experiments in Interstellar photoprocessing system (IPS) [5], an ultra-high vacuum chamber with base pressure  $3 \times 10^{-10}$  torr. By ideal gas law, the pressure corresponded to a density of  $2 \times 10^8$  molecules  $\text{cm}^{-3}$ , which is similar to dense cloud interiors. We would like to particularly simulate the surface of Charon. The surface pressure of Charon is however not specific to high VU cross-section gases are not well defined yet, which will be in a future report by New horizons team, while all known species in Pluto's atmosphere to be below 0.3 nano bars ( $2.25 \times 10^{(-7)}$  torr) [12]. The system will be introduced in detail in section 2.1.1. To simulate the irradiation in interstellar environments, we use a micro-wave discharge hydrogen lamp (MDHL) and monochromatic extreme-ultraviolet irradiation (EUV) 30.4 nm (40.8 eV) to irradiate our ice mixtures, and these will be introduced in section 2.1.2 and 2.1.3 respectively. The experimental protocols will be elaborated in section 2.2. For some non-physic background readers, basic theories of Infrared spectroscopy and basic chemical kinetics used in data analysis are included in section 2.3 and 2.4 respectively.

#### 2.1.1 Experimental simulations by IPS system

We conduct our astrophysical simulations in Interstellar Photo Processing System (IPS) (figure 2.1). IPS consists in three systems: the main chamber, where our experiments take places; the detection system, where we collect our data; and a gasline system, where we prepare our samples.

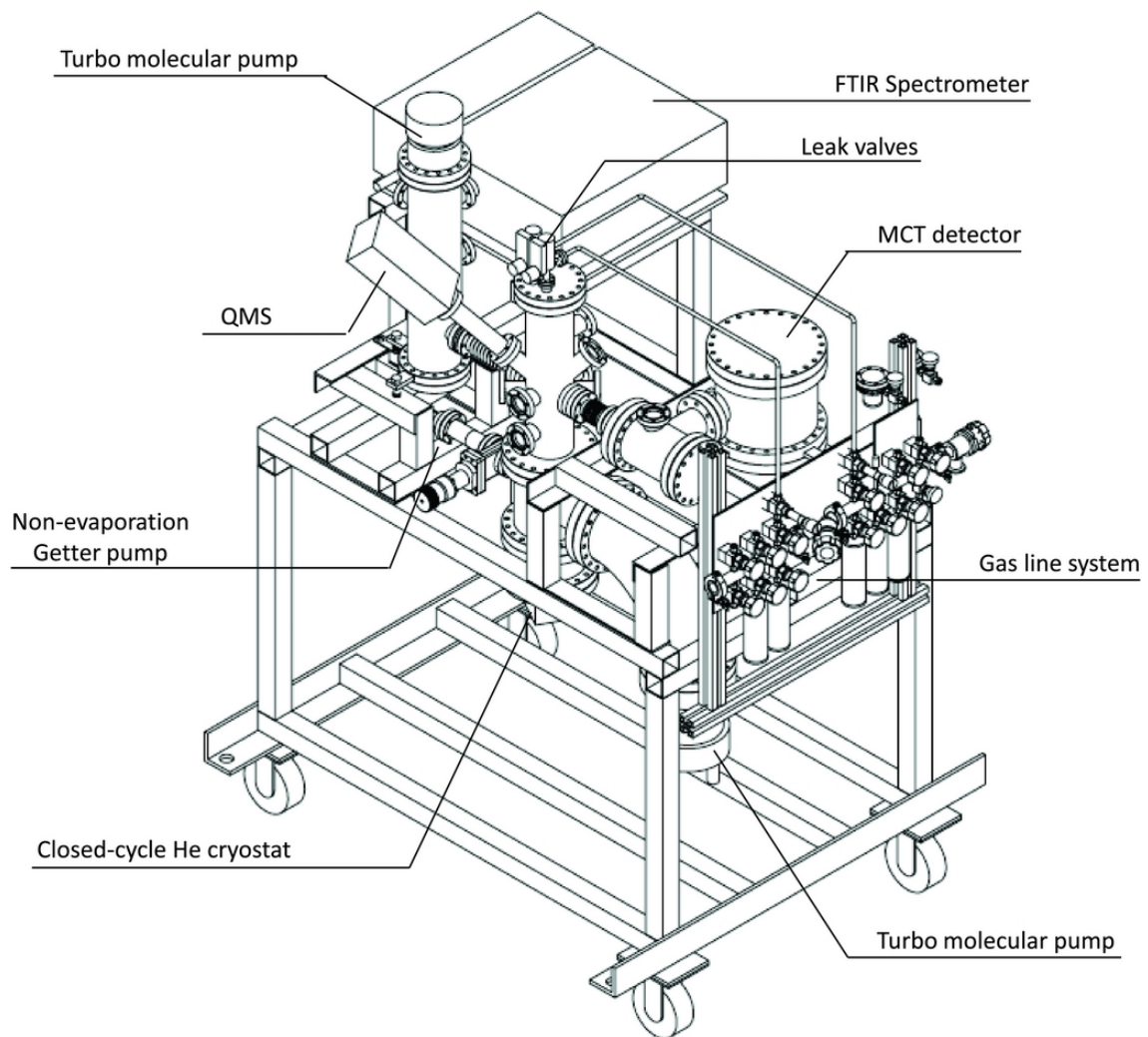


Figure 2.1: The schematic diagram of IPS system, mechanical pumps are not shown for clarity. (Quoted from Chen et al. 2014)



The main system consists of an ultrahigh vacuum chamber equipped with a closed-cycle helium cryostat (CTI-M350). It is pumped by a turbo molecular pump, which is backed up by a scroll pump, and a non-evaporation getter pump. The getter pump, with a larger surface area, is a powerful tool to adsorb residue gases ( $\text{H}_2$ ,  $\text{CO}$  and  $\text{N}_2$ ) inside the main chamber, which can obtain a better base pressure. After baking, the base pressure of our main chamber can reach  $1 \times 10^{-10}$  torr at 15 K, monitored by a Granville-Phillips 370 Stabil-Ion gauge. This pressure can be used to simulate the dense cloud interior environments and star forming region. The substrate we have chosen is KBr, which is transparent to infra-red photons with 700 to 4000  $\text{cm}^{-1}$ . It is mounted by substrate holder (oxygen-free copper), on the second stage of cold finger, which is on the tip of cryostat. A silicon diode and a heater are placed onto the cold finger, and another silicon diode is placed on the substrate holder. They are connected to a temperature controller and PID (proportional-integral-derivative controller) system to achieve a warmup rate of 1K/min with an accuracy of 0.1 K.

The detection system consists of a mid-infrared Fourier transform spectrometer (mid-FTIR) (ABB FTLA2000-104) and a Quadrupole Mass Spectrometer (QMS). To prevent absorption bands of  $\text{CO}$ ,  $\text{CO}_2$  and  $\text{H}_2\text{O}$  gas from the atmosphere, the IR beam path is built inside vacuum, pumped by dry pump. The main chamber and the IR path are separated by ZnSe windows, allowing infra-red penetration from 0.5 – 20  $\mu\text{m}$  with absorption less than 0.07 %. In this study, the infrared spectra are obtained with resolution of 4  $\text{cm}^{-1}$  and averaged over 32 scans. The angle between the IR beam path and the substrate holder is 45 degrees. The QMS (MKS Microvision 2) consists of a controller and mechanical part sealed by a mounting flange in ultrahigh vacuum. It is mounted 10 cm from the substrate and runs with a resolution 0.5 a.m.u. The ionizer releases 70 eV electron by filament and ionizes incoming molecules to positive charged ions between anode grid and repeller. The ions are accelerated by focus plate and enters ion filter, which consists of four circular rods, with a combination of A.C and D.C. potential to sieve whole bandpass ions at millisecond timescale. The selected ions

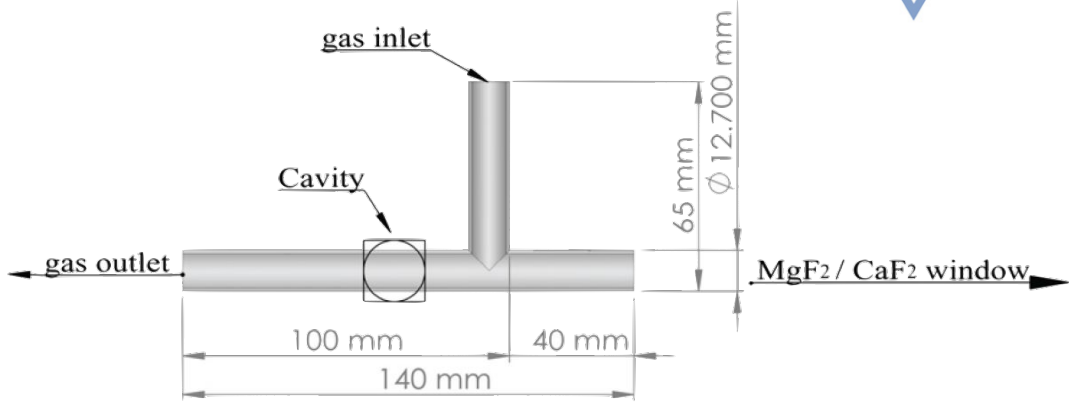


Figure 2.2: The cross-section of MDHL (T-type geometry) (Quoted from Chen et al. 2014).

enter ion detector and are detected by either faraday cup and continuous dynode electron multiplier (CDEM) which can multiply weak signals.

The samples are prepared in situ in our gasline system. It contains four stainless steel bottles with the same volume, which is used to determine relative proportion of the gas mixtures by their partial pressures. The ammonia gas (4N) and methane gas (5N) are mixed with partial pressure measured by a Baratron (0 - 100 torr) with a 0.25% accuracy. The background pressure of the gasline system is lower than  $1 \times 10^{-7}$  torr, thanks to a turbomolecular pump (Oerlikon Leybold TurboVac 151, capacity 145 liters s<sup>-1</sup>). It is backed up with a mechanical pump (Alcatel 2012A, capacity 450 *litersminute*<sup>-1</sup>), equipped with an oil trap (molecular sieve type 13X).

### 2.1.2 Vacuum-UV source

In order to simulate the photoprocessing of vacuum ultraviolet (VUV) irradiation of the interstellar ices and ices on planetary bodies, including Kuiper Belt Objects (KBO), the ice mixtures are irradiated with a T-type Microwave-Discharged Hydrogen-flow lamp (MDHL) isothermally. Figure 2.2 shows a cross-section of T-type quartz tube; the middle part of the T-type quartz tube is being tunned by a ceramic rod that is called Evenson cavity. The molecular hydrogen with pressure 0.4 torr flows through the lamp with a support of a mechanical pump. Using a microwave generator and high voltage discharge, a low pressure plasma is produced in the Evenson cavity. In order to measure the photon flux

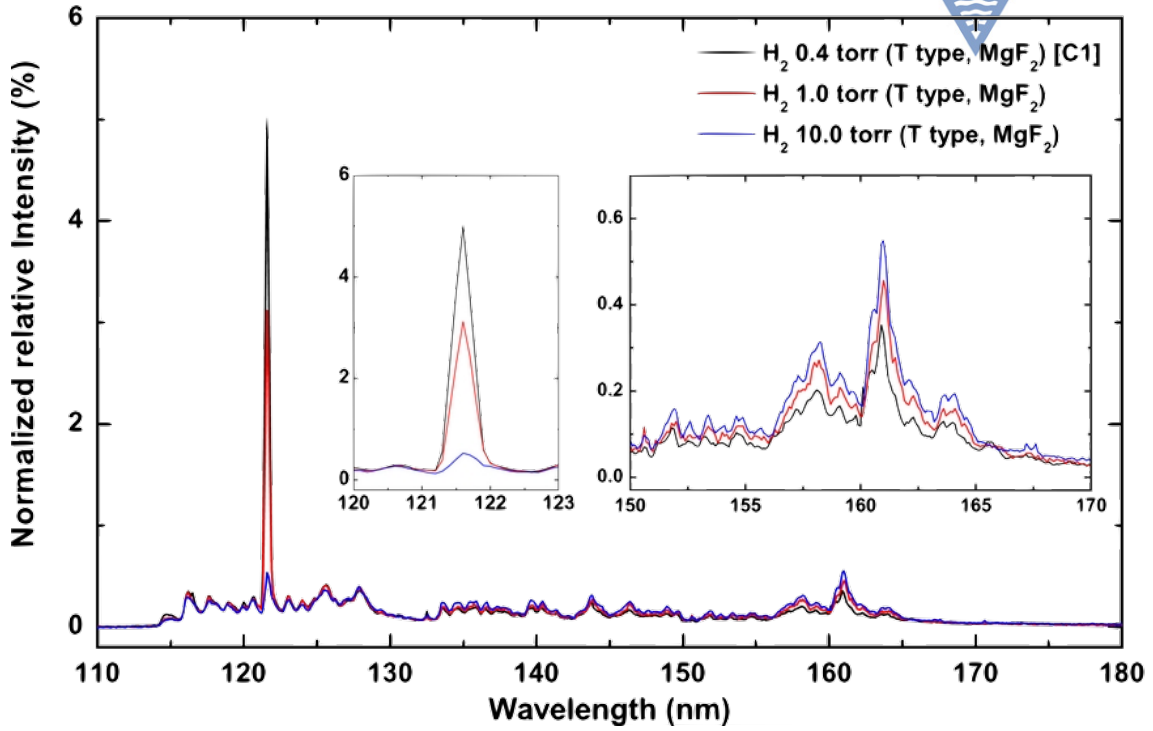
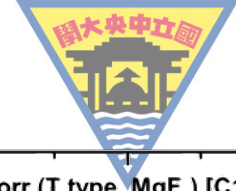


Figure 2.3: VUV spectra of MDHL (T-type geometry, 110-180 nm) with different  $H_2$  pressure inside the lamp(Quoted from Chen et al. (2014)[5]) .

in situ, we use an 88 % transmittance nickel mesh with its photoelectric efficiency being obtained by high-flux beamline in National Synchrotron and a SXUV 100 photodiode calibrated by NIST. A  $MgF_2$  window is placed between the lamp and the sample holder to prevent penetration of higher order VUV photons (with wavelength shorter than 114 nm). Figure 2.3 shows a VUV emission spectrum of a MDHL with a cut off at 114 nm. It consists of  $Ly-\alpha$  (121.6nm) photons and  $H_2$  molecular emission in the range of 110-180 nm. Chen et al. (2014) showed that the spectral characteristics of the VUV light emitted in this range depends on the gas type (mixture of  $H_2$  with He or Ar etc), pressure of  $H_2$  and lamp geometry [5]. Throughout those configurations stated there, we adopted 0.4 torr molecular hydrogen and T-type MDHL that produces VUV irradiation at 114-170 nm with 19.1 % of  $Ly-\alpha$  photons and a mean photon energy of 9.27 eV. The photon flux is  $6.4 \times 10^{13}$  photons  $cm^{-2}s^{-1}$  at sample position.



### 2.1.3 Extreme EUV source

To simulate the solar EUV irradiation on both Charon and interstellar ices, we use the HF-CGM high – flux beam line of the National Synchrotron Radiation Research Center in Hsinchu, Taiwan. It provides a continuum EUV to VUV photons from 4 to 40 eV. The continuum is separated into monochromatic 30.4nm (40.8 eV) photons with a six-meter cylindrical grating monochrometer with an incident angle of 70 degrees. With the help of a movable entrance slit and movable curved exit slit, the energy resolving power can reach around  $3 \times 10^4$  at 40 eV for grating 1600 l/mm with both slits movable and set opening to  $10 \mu\text{m}$  [13]. Similar to VUV irradiation provided by MDHL, the light intensity is monitored by the same nickel mesh with photoelectric efficiency obtained by SXUV 100 photodiode calibrated by NIST. With the known photoelectric efficiency, the flux of monochromatic 30.4nm (40.8 eV) is measured to be  $2.15 \times 10^{14} \text{ photons } s^{-1} \text{ cm}^{-2}$ , which is in the same order of magnitude of VUV continuum of MDHL. We replace the port with MDHL by the end station of the high-flux beamline. To prevent contaminations in the pipes and bellows, we place a cryostat backed up by a scroll pump between our system and the beamline endstation. Between the cryostat and our main chamber is a  $\text{SiO}_2$  valve, which is sealed to prevent contamination to the end station during the warm-up phase.

## 2.2 Experimental Protocol

In this section, we will briefly introduce the procedures of how we perform our experiments. It is divided into four parts, preparation and cooling, deposition, irradiation and warmup.

### 2.2.1 Preparation of experiments and cooling

Before any of experiment is done, we bake our system at  $100^\circ\text{C}$ , for 48 hours to reduce the contamination of water and residue gases as much as possible. It is cooled to room temperature that the background pressure can reach routinely at  $1 \times 10^{-10}$  torr. The gasline is connected with the regulators of the gas tanks and bake to  $100^\circ\text{C}$  and pumped by turbomolecular pump for two days before any experiments are done.





Before cooling the substrate to cryogenic temperature, we take an infrared(IR) spectrum and start the monitoring of residue gases by QMS in order to compare the residue molecules and to verify any possible contaminations in the main chamber. We then start the cooling process with the help of the closed-cycle He cryostat.

### 2.2.2 Deposition

The gas mixtures are pre-mixed in our gasline system introduced in section 2.1.1. We control the relative proportion of two ice mixtures by sealing corresponding partial pressure gases in two equal volume stainless steel bottles. We condense the gas premixed in the stainless steel bottles onto pre-cooled KBr substrate via leak valve. The substrate is monitored by Fourier-Transform Infrared (FTIR) Spectrometer and Quadrupole mass spectrometer (QMS) during deposition. The pressure of deposition is fixed to  $1 \times 10^{-8}$  torr that the deposition rate is around  $4 \times 10^{16}$  molecules  $\text{cm}^{-2} \text{min}^{-1}$ , which varies in different relative ratio of our ice mixtures because the differences in sticking coefficients. After deposition, we place the ice mixture at 15 K for 60 minutes and allow pumping of residue gases, until the pressure of the main chamber falls back to its base pressure to simulate the interstellar environment before any irradiation.

### 2.2.3 Photon Irradiation

The total irradiation time is 270 minutes (with some 450 minutes, depend on experiment configurations) with time intervals varies from 2 to 30 minutes. After each irradiation, we wait for 10 minutes allowing pumping out of the photodesorbed gas molecules. During irradiation, the photon flux is monitored by a nickel mesh. After Irradiation, we place the sample for 30 minutes in case if any further reaction is processed.

### 2.2.4 Warmup

We heat the tip of cold finger to 300 K (measured by silicon diode near the substrate) with rate 1 K/min. During warmup, we record the QMS from 1 to 100 a.m.u. to observe if there are low quantity of higher



mass products formed during irradiation. Apart from QMS, we scan infrared spectra with 5 K intervals to monitor the evolution of infra-red active species such as photo products and reactants. With both infra-red and QMS, we may better identify the photo products by kinetic energy gained during warm-up and temperatures the desorpted.

## 2.3 Infra-red spectroscopy and the Beer-Lambert's Law

We use infra-red spectroscopy extensively in chapter 3. It is a powerful tool to study molecular interactions during irradiation and warmup. We choose infra-red rather than Raman spectroscopy because infra-red has lower energy that it would not change the structure of the ice mixture nor breaking any of the bonds. In addition, it is also much richer in terms of identifying functional groups especially when studying ice mixtures whose vibrational modes falls in the mid-IR wavelength ranges. With different vibrational modes, the energy absorbed by molecules are quantified. With the energy of absorption bands in infra-red spectrum, we may identify the functional group of the species. To simply classify, vibrational motions can be divided into stretching and bending. Stretching needs more energy than bending. For stretching, there are symmetric and asymmetric stretchings; while bending can be divided into in-plane (scissoring, rocking) and out-of-plane (wagging and twisting) (Figure 2.4).

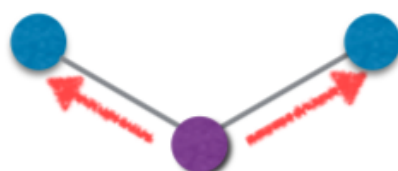
By Beer's Law, we may calculate the column density of the molecule with its functional groups, which are used to plot figures in chapter 3 and 4. Beer Lambert's Law suggests that when light passes through a medium, the amount of light absorbed is proportional to density and path length of the medium. Assume a known intensity beam  $I_0(\nu)$  passes through the medium and beam intensity become  $I(\nu)$ . The transmittance  $T(\nu)$  is defined by equation 2.1.

$$T(\nu) = \frac{I(\nu)}{I_0(\nu)} \quad (2.1)$$

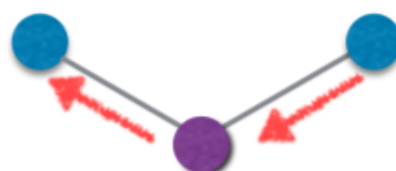
Also, the absorbance  $a(\nu)$  is defined by equation 2.2.

$$a(\nu) = -\ln T(\nu) = -\ln \frac{I(\nu)}{I_0(\nu)} = nl\sigma(\nu) \quad (2.2)$$

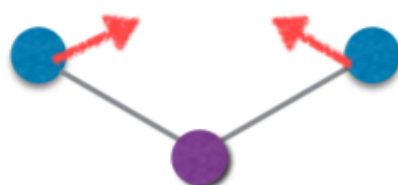




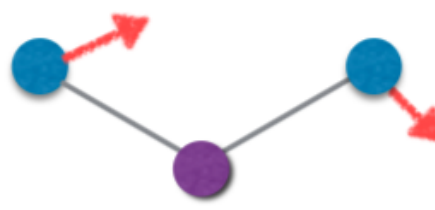
Symmetric



Asymmetric



In-plane Scissoring



In-plane Rocking



Out of plane Wagging



Out of plane Twisting



 indicate motion out of the page  
 indicate motion into the page

Figure 2.4: Different vibrational modes of a three atom molecule.



where  $n$  is number density (molecules/cm<sup>3</sup>),  $l$  is the path length (cm),  $\sigma(\nu)$  is the cross-section (cm<sup>2</sup>/molecule) of corresponding frequency  $\nu$ . This equation is known as Lambert Beer's Law.

As the ice mixtures in our thesis are at 15 K, the peaks of absorbance are often a broadband due to coupling between neighbor molecules. Therefore, we can integrate the whole band of the peak by equation 2.2 with respect to frequency. Combines the (integrated) absorbance band strength (A value) in literatures to calculate the column densities  $N$  of the ices by equation 2.3.

$$N = \frac{\int a(\nu) d\nu}{A(\nu)} \quad (2.3)$$

where  $N$  is the column density (molecule cm<sup>-2</sup>),  $A(\nu)$  is the absorbance strength (cm molecule<sup>-1</sup>).

## 2.4 Reaction Rate Laws

In this section, we will introduce rate reaction of a consecutive reaction and the concept of pseudo first order which we use to fit our reaction product against photon dose in chapter 3. The rate of a chemical reaction is a change in concentration of a substance per unit of time.

To determine the order of a reaction, we can only determine it experimentally. For a zero order reaction, the rate =  $-\frac{d[R]}{dt} = k[R]^0$ . By calculus,  $[R]_0 - [R]_t = kt$ .

For a first order reaction, rate =  $-\frac{d[R]}{dt} = k[R]$ . By calculus,  $\ln[R]_t = -kt + \ln[R]_0$ .

For a second order reaction, rate =  $-\frac{d[R]}{dt} = k[R]^2$ . By calculus,  $\frac{1}{[R]_t} - \frac{1}{[R]_0} = kt$ .

In a reaction with one reactant in excess, the rate of reaction is called pseudo first order reaction where pseudo means pretended. For  $D+E \rightarrow F$ , rate =  $k[D][E]$ . As  $[E]_0 \gg [D]_0$ , change of  $[E]$  is negligible that  $[E] \sim [E]_0$ . Therefore,  $[E]$  is assumed to be a constant and included in the rate constant  $k$ .

For a consecutive reaction equation, which we used to fit our data points, where  $D \rightarrow E \rightarrow F$  that the produced product will not convert



back as reactant. A simple example is radioactive decay. At  $t = 0$ ,  $[D] = [D]_0$ ,  $[E] = 0$ ,  $[F] = 0$  and at all times,  $[D] + [E] + [F] = [D]_0$ . The rate equations are as follows:

$$\frac{d[D]}{dt} = -k_1[D] \quad (2.4)$$

$$\frac{d[B]}{dt} = k_1[D] - k_2[E] \quad (2.5)$$

$$\frac{\Delta[F]}{\Delta t} = k_2[E] \quad (2.6)$$

By equation 2.4, we get

$$[D] = [D]_0 e^{-k_1 t} \quad (2.7)$$

By substituting equation 2.7 into equation 2.5, we get

$$-\frac{\Delta[E]}{\Delta t} + k_2[E] = k_1[D]_0 e^{-k_1 t} \quad (2.8)$$

After solving the differential equation 2.8, we get

$$[E] = \frac{k_1}{k_2 - k_1} (e^{-k_1 t} - e^{-k_2 t}) [D]_0 \quad (2.9)$$

Finally, since  $[F] = [D]_0 - [E] - [D]$ , by equation 2.7 and 2.9, we get

$$[F] = \left( 1 + \frac{k_1 e^{-k_2 t} - k_2 e^{-k_1 t}}{k_2 - k_1} \right) [D]_0 \quad (2.10)$$



## 3. Results and Discussions

In this chapter, we will investigate the following mainly by infrared spectroscopy: 1. The photoproducts produced by different concentration ratios of methane to ammonia, 2. the reaction mechanisms of each main products, 3. the photo products produced by EUV and VUV photons and 4. the functional groups of tholin formed by irradiation of VUV, EUV on different relative proportions of  $\text{CH}_4:\text{NH}_3$  ice mixtures (the result is compared with the residues on Titan produced by Imanaka et al. [14]).

### 3.1 The infrared spectra and peaks identification

Figure 3.1 is a typical infrared spectrum of  $\text{CH}_4:\text{NH}_3$  ice mixtures in different concentration ratios: 1:20, 1:10, 1:5 and 3:2 where ammonia is fixed with a column density  $6 \times 10^{17}$  molecules  $\text{cm}^{-2}$ . We scan the IR spectrum prior to the irradiation at 15 K (for details of methodology, please refer to section 2.2).

Table 3.1: The strength of absorbance adopted in this thesis measured in literatures of pure ice samples

Wavenumber ( $\text{cm}^{-1}$ )	Assignment	Vibration	FWHM	A value ( $\times 10^{-17}$ )	Reference
2976	$\text{C}_2\text{H}_6$	$-\text{CH}_3$	-	1.05	2
2960	$\text{C}_3\text{H}_8$	$-\text{CH}_2-$	-	2.58	2
2086	$\text{CN}^-$	CN	-	1.8	3
1297	$\text{CH}_4$	CH deformation	8	0.61	1
1070	$\text{NH}_3$	"umbrella mode"	68	1.7	1

Reference: 1. d'Hendecourt and Allamandola (1986)[6] 2. Moore and Hudson (1998)[15] 3. Noble et al. (2013) [16]

The peaks used in column density calculations (by equation 2.3) are labelled by dotted lines in the graph (figure 3.1). We are aware that IR absorption strengths can vary depending on its environment, which means it will be different when it is pure, when it is mixed with other

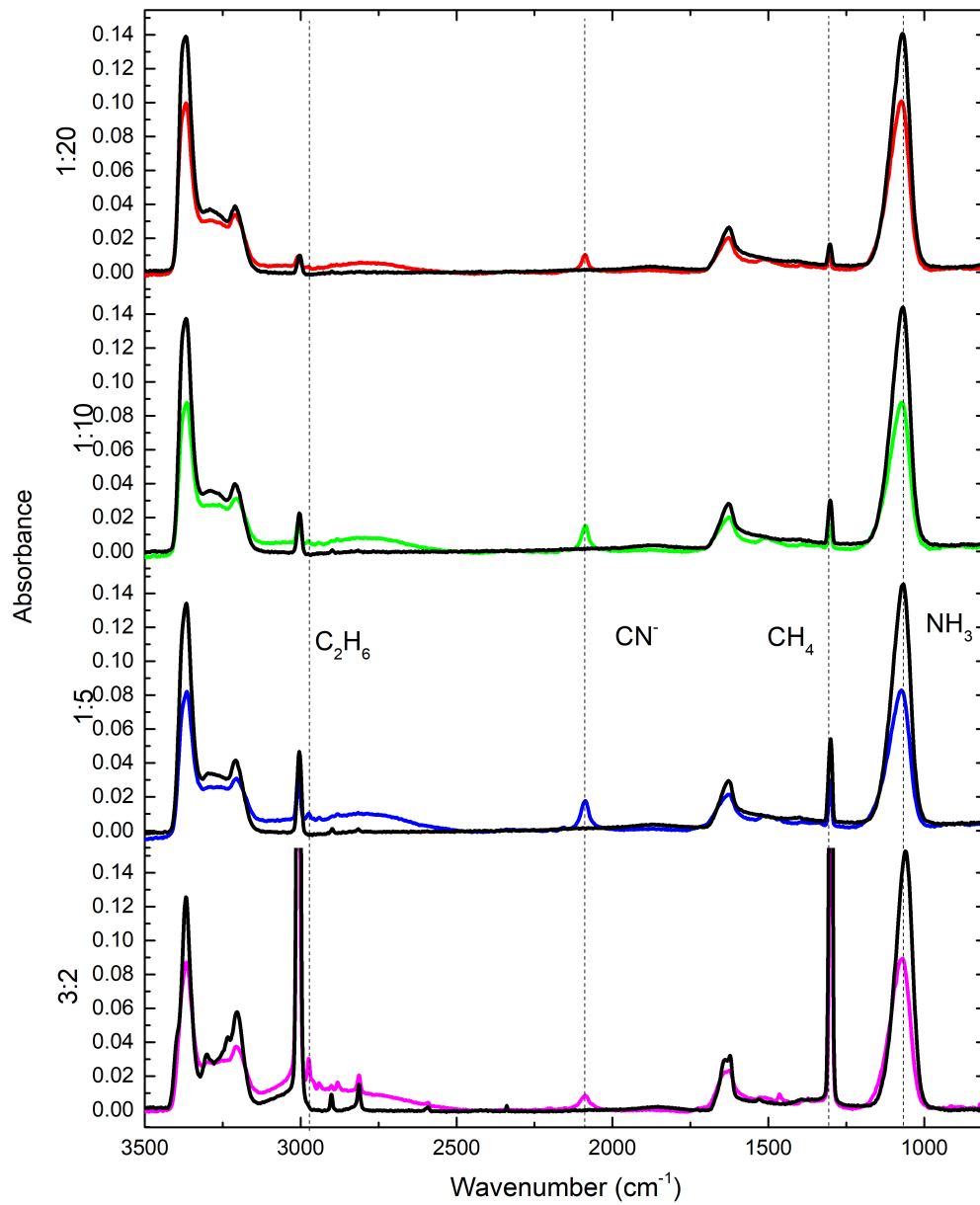


Figure 3.1: The the infrared spectrum of  $\text{CH}_4 + \text{NH}_3$  ice mixtures before irradiation (black) and after VUV (MDHL) irradiated (coloured) ice mixtures.



ices, and will vary with the relative proportions between ice components. We are justified to use the same absorption strength throughout our discussion to estimate the column density of each species and how the absorption area changes with concentration ratios of ice mixtures and photon energy. The absorption strengths we adopted are stated in table 3.1

Figure 3.2 is a zoomed view of figure 3.1. Multiple peaks are used in product assignments, which are presented in table 3.2. The absorption peak located at  $2975\text{ cm}^{-1}$  corresponds to the strongest vibration of  $\text{C}_2\text{H}_6$ .

The peak positioned at  $2960\text{ cm}^{-1}$  belongs to  $-\text{CH}_2-$  so we tentatively assign that as  $\text{C}_3\text{H}_8$ , which is the shortest carbon chain molecule contains  $-\text{CH}_2-$ . By fitting the peaks as a few gaussians, we deconvolute the overlapped  $\text{C}_2\text{H}_6$  and  $\text{C}_3\text{H}_8$  into two gaussians. The signal-to-noise ratio in  $\text{CH}_4:\text{NH}_3 = 1:10$  is poor that we can not quantify the amount of  $\text{C}_3\text{H}_8$  (figure 3.2).

Figure 3.3 is zoomed infrared absorption spectra of  $\text{CN}^-$ . We assign the peak  $2086\text{ cm}^{-1}$  to  $\text{CN}^-$  but not a combination of HCN and  $\text{CN}^-$ . The assignment is based on a absence in CN bending mode at  $848\text{ cm}^{-1}$ . In the case  $\text{CH}_4 + \text{NH}_3 = 3:2$ , we may observe a peak located at  $820\text{ cm}^{-1}$ , the characteristic of the band is different from HCN (halved FWHM of HCN) and it is eliminated at 50 K during the warm-up phase. Since 50 K is the desorbing temperature of  $\text{C}_2\text{H}_6$  and the peak position is close to  $\nu_{12}$  mode of  $\text{C}_2\text{H}_6$ , we believe that the  $820\text{ cm}^{-1}$  peak is contributed by  $\text{C}_2\text{H}_6$ . Therefore, we may assign our peak located at  $2086\text{ cm}^{-1}$  as purely  $\text{CN}^-$ . After identification of the main products ( $\text{C}_2\text{H}_6$ ,  $\text{CN}^-$  and  $\text{C}_3\text{H}_8$ ), we will look into the mechanisms one by one in the next section.

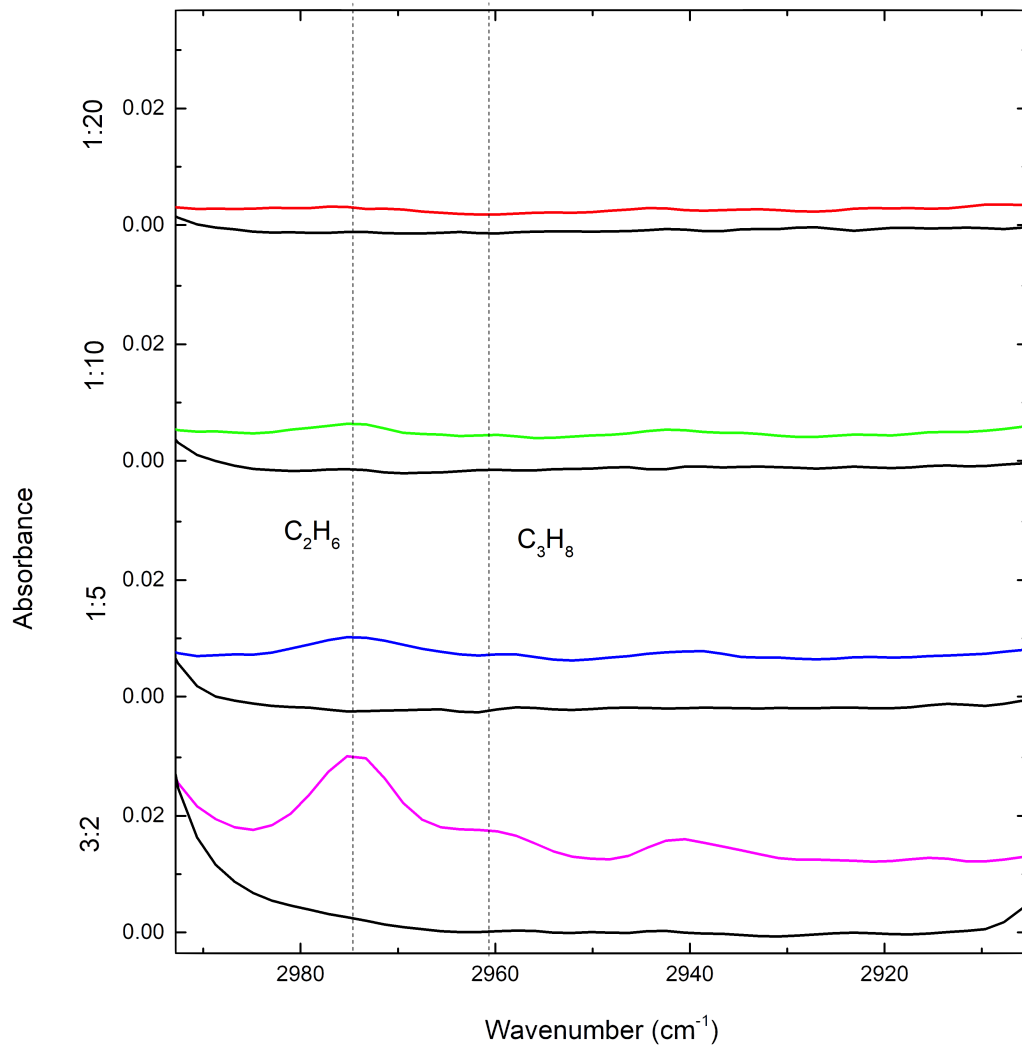


Figure 3.2: The infrared spectra of  $\text{CH}_4 + \text{NH}_3$  ice mixtures in the range of  $\text{C}_2\text{H}_6$  and  $\text{C}_3\text{H}_8$  vibrations before irradiation (black) and VUV irradiated ice mixtures provided by MDHL.

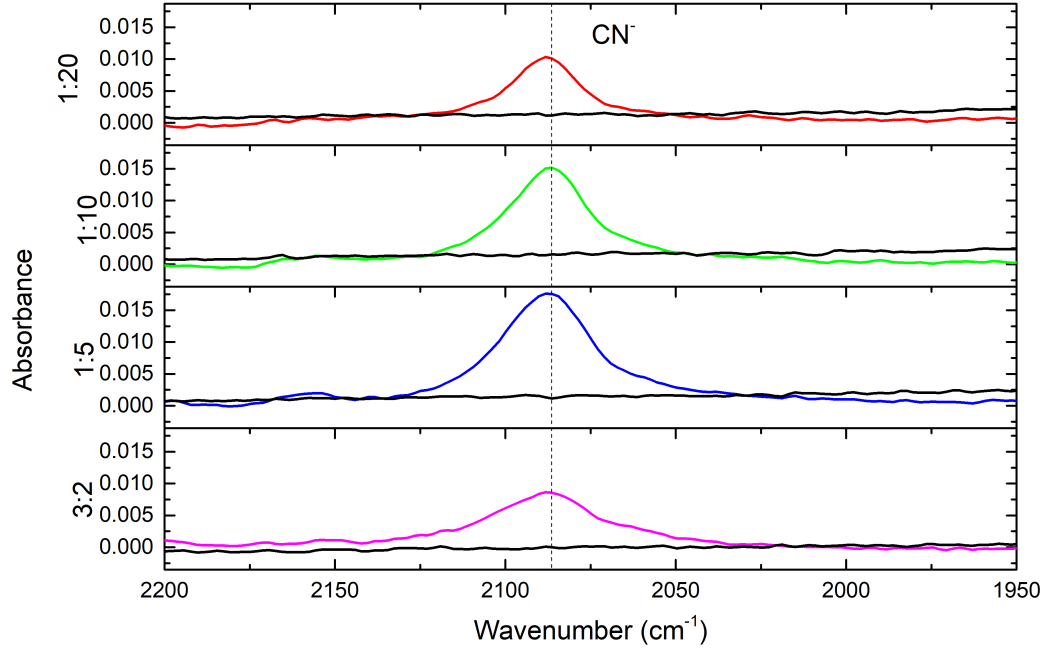


Figure 3.3: The infrared spectrum of  $\text{CH}_4 + \text{NH}_3$  ice mixtures of  $\text{C}_2\text{H}_6$  and  $\text{C}_3\text{H}_8$  before irradiation (black) and VUV irradiated ice mixtures provided by MDHL.

Table 3.2: The peak positions of identified substances after irradiation in different relative proportions of ice mixtures.

Literature assignments		$\text{CH}_4:\text{NH}_3$ ratio (MDHL)				Ref.
Wavenumber ( $\text{cm}^{-1}$ )	Identified IR modes	1:5 ( $\text{cm}^{-1}$ )	1:10 ( $\text{cm}^{-1}$ )	1:20 ( $\text{cm}^{-1}$ )	3:2 ( $\text{cm}^{-1}$ )	
3375	$\nu_3$ ( $\text{NH}_3$ )	3366	3366	3369	3367	1
3210	$\nu_1$ ( $\text{NH}_3$ )	3207	3208	3210	3205	1
2972	$\nu_{10}$ ( $\text{C}_2\text{H}_6$ )	2975	-	-	2975	3
2960	$\text{C}_3\text{H}_8$	-	-	-	2960	7
2941	$\nu_8 + \nu_{11}$ ( $\text{C}_2\text{H}_6$ )	2940	-	-	2940	3
2904	$\nu_1$ ( $\text{CH}_4$ )	2901	-	-	2901	5
2879	$\nu_5$ ( $\text{C}_2\text{H}_6$ )	2882	2883	-	2882	3
2814	$\nu_2 + \nu_4$ ( $\text{CH}_4$ )	-	-	-	2815	5
2083	$\nu$ ( $\text{CN}^-$ )	2088	2087	2088	2088	2
1625	$\nu_4$ ( $\text{NH}_3$ )	1625	1625	1626	1631	1
1514	$\delta$ ( $\text{NH}_2$ )	1509	1507	1505	1511	6
1465-1440	deform $\text{CH}_2$ scissor	1461	-	-	1463	3,4
1390-1370	$\text{CH}_3$ sym deform	1394	1394	1394	1372	4
1298	$\nu_4$ ( $\text{CH}_4$ )	1301	1302	1305	1299	2
1075	$\nu_2$ ( $\text{NH}_3$ )	1073	1072	1072	1072	1
820	$\nu_{12}$ ( $\text{C}_2\text{H}_6$ )	-	-	-	820	3

Reference: 1. Bossa et al. 2008 [17] 2. Moore and Hudson 2003 [18] 3. Kim et al. 2010 [19] 4. Socrates 2001 [20] 5. Bennet and Kaiser 2007 [21] 6. Zheng et al. 2008 [22] 7. Hudson and Moore 2004 [23]





## 3.2 Reaction mechanisms and fitting results

### 3.2.1 $C_2H_6$

The formation of  $C_2H_6$  in astrophysical environment is mainly a combination with 2  $CH_3$  radicals [24]:



The energy requires to break the CH bond of  $CH_4$  is 4.42 eV. The recombination of 2  $CH_3$  radicals forms a internal excited  $C_2H_6$ , and releases 3.74 eV to the surrounding matrixs or proceeds further to become ethly radicals ( $C_2H_5$ ) or ethene ( $C_2H_4$ ) (required extra of 0.53 and 0.84 eV respectively. [24]. Therefore, the process in equation 3.2 is a no-barrier exothermic process. The formed  $C_2H_6$  is internally excited that it is able to become  $C_2H_4$  etc. Figure 3.4 depicts the formation column density as a function of irradiation time of  $C_2H_6$  in different relative proportions of irradiated ice mixtures. As the formation only depends on  $CH_4$ , we may use first order kinetics equation to fit the column density versus photon dose.

$$[C_2H_6] = [C_2H_6]_0(1 - e^{-kt}) \quad (3.3)$$

The fitting results are shown in table 3.3. From table 3.3, the production rate is nearly proportional to the initial  $CH_4$  concentrations. Note that  $C_2H_6$  is not detected in  $CH_4$  to  $NH_3 = 1:20$  ice mixtures.

Table 3.3: The fitting results of  $C_2H_6$  by  $[C_2H_6] = [C_2H_6]_0(1 - e^{-kt})$

Ratio of $CH_4:NH_3$	$[C_2H_6]_0$ ( $\times 10^{15}$ molecules $cm^{-2}$ )	$k$ ( $\times 10^{-17}$ photon $^{-1}$ )
1:10	$2.90 \pm 1.25$	$0.92 \pm 0.15$
1:5	$4.16 \pm 0.28$	$2.28 \pm 0.28$
3:2	$19.2 \pm 0.15$	$5.28 \pm 0.25$

### 3.2.2 $C_3H_8$

Propane is a secondary product formed by a combination of either  $C_2H_6 + CH_2$  (equation 3.4) or  $C_2H_4 + CH_4$  (equation 3.5). From Bennet

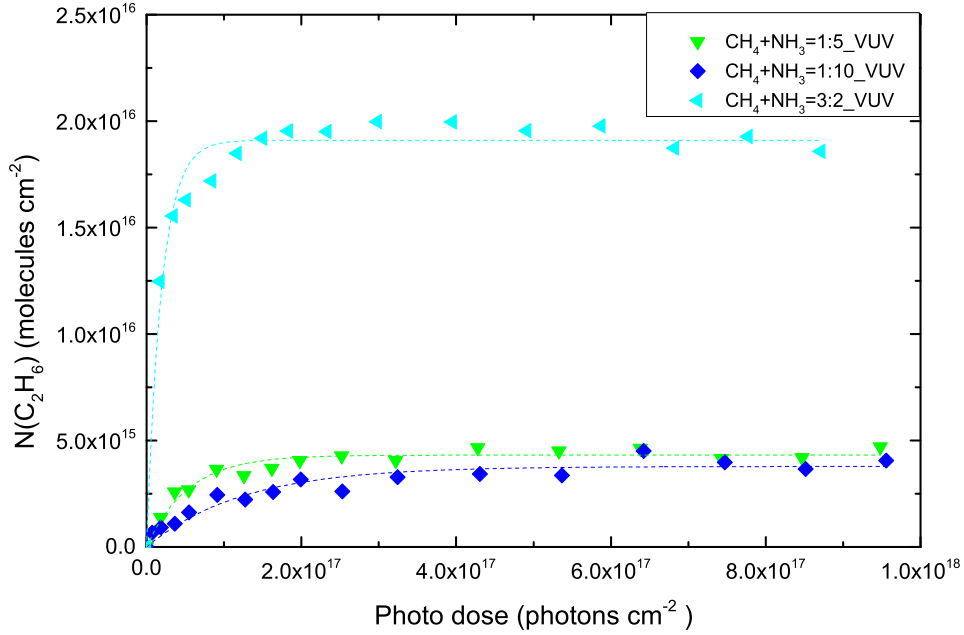


Figure 3.4: The column density of  $C_2H_6$  during  $CH_4 + NH_3$  ice mixtures irradiated by MDHL.

et al. (2006) [24],  $C_2H_4$  is decomposed by the internally excited  $C_2H_6$ . With subsequently impinging electrons, it is degraded into  $C_2H_3$  and  $C_2H_2$  with an energy barrier of 4.69 and 4.06 eV respectively.



Table 3.4: The fitting results of  $C_3H_8$  by  $[C_3H_8]=[C_3H_8](1 - e^{-k_1t})$

Ratio of $CH_4:NH_3$	A ( $\times 10^{15}$ molecules $cm^{-2}$ )	k ( $\times 10^{-17}$ photon $^{-1}$ )
1:5	$0.46 \pm 0.17$	$2.89 \pm 2.44$
3:2	$3.84 \pm 0.18$	$2.08 \pm 0.18$

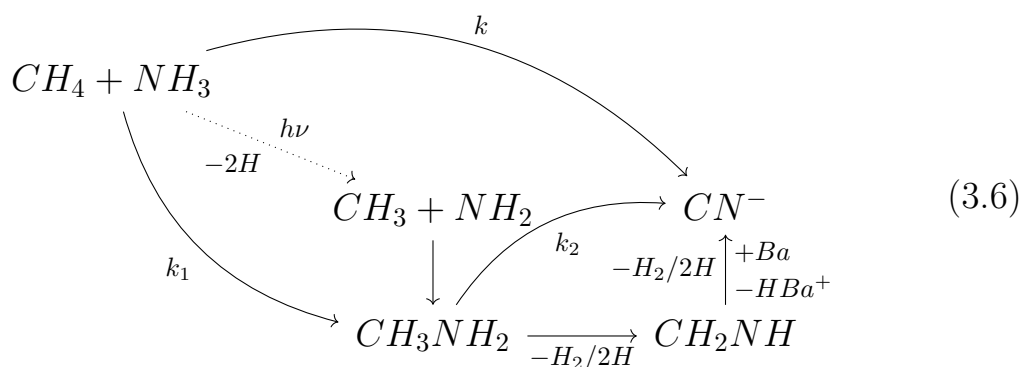
The column densities are shown in figure 3.5, where the fitting results are shown in table 3.4. Since the  $C_3H_8$  detection in  $CH_4 + NH_3 = 1:5$  ice mixtures are close to our detection limits, the errors of the fitting results would attributes to a meaningless fitting.

### 3.2.3 $CN^-$

The formation mechanism of  $CN^-$  at low temperature was suggested by Kim and Kaiser (2011) to be two step reaction mechanism



Figure 3.5: The column density of  $\text{C}_3\text{H}_8$  during  $\text{CH}_4 + \text{NH}_3$  ice mixtures irradiated by MDHL.



Kim and Kaiser (2011) used 1.5 keV electron as energy source to simulate the cosmic ray induced photochemistry [2]. Despite the extra heats generated in these exothermal reactions:



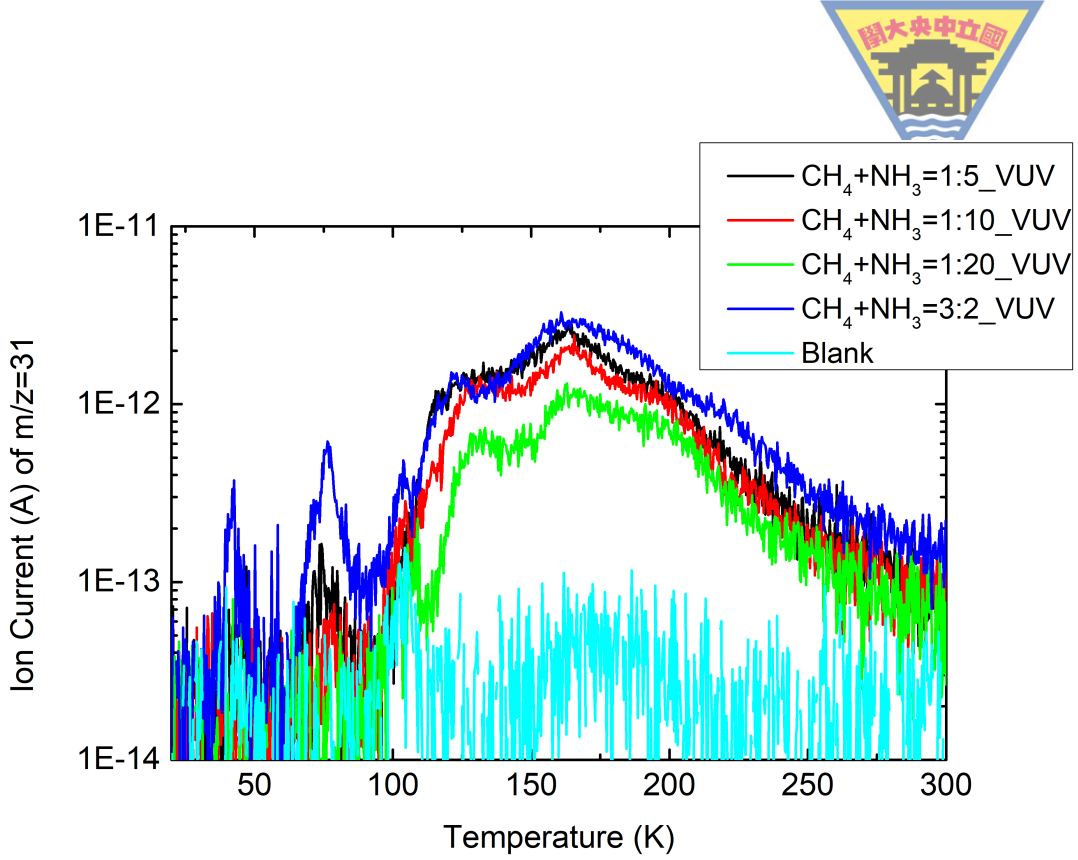


Figure 3.6: The ion current with mass to charge ratio 31 detected by QMS during warm-up with heating rate 1 K/min in different relative proportions of ice mixtures.



Kundu et al. (2017) fails to observe methylamine as intermediate during warmup phase after using 1–90 eV electrons to initiate  $CH_4$  and  $NH_3$  ice mixtures[11]. The non-detection is probably due to their thin ice thicknesses (just a few monolayers). This formation mechanism also applies in our photon irradiation experiments because we can also detect the methylamine during our warm-up phase. The ion fragment with  $m/z=31$  is assigned as  $CH_3NH_2^+$  and detectable in all ratios of our  $CH_4 + NH_3$  experiments (figure 3.6).

Mentioned in section 2.4, we use rate equation for consecutive reactions 2.10 to fit our  $CN^-$  column densities. This rate equation applies in our experiments with one of the reactants in excess. Since  $CH_4$  is more abundant than  $NH_3$  ( $CH_4:NH_3=3:2$ ); or  $NH_3$  is in excess ( $CH_4:NH_3 = 1:5, 1:10$  and  $1:20$ ) we may apply the pseudo first order assumption. Throughout the formation mechanism, one of the reactant (niether C or N) is a limiting reatant, therefore, we may apply the rate equation 2.10

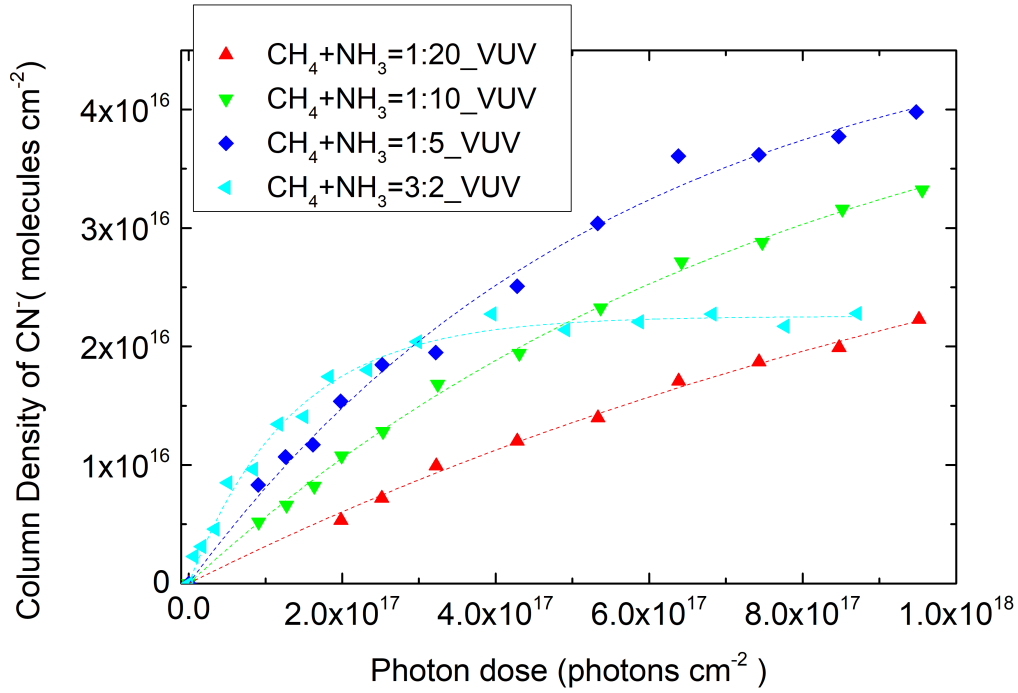


Figure 3.7: The column density of  $\text{CN}^-$  accumulated when different relative proportions of  $\text{CH}_4 + \text{NH}_3$  ice mixtures are irradiated by VUV photons provided by MDHL. The dotted lines are fits of column densities by equation 2.10.

to fit the formation of  $\text{CN}^-$  (figure 3.7).

The fitting results are averaged by more than two experiments and are shown in table 3.5. We find that one of the rate constant is always larger than the other in all of the ratios. The results of Kim and Kaiser (2011) is also listed into the table, they could observe a two-step reaction mechanism in production of  $\text{CN}^-$  in  $\text{CH}_4:\text{NH}_3 = 3:1$  experiments with electron current  $0.1 \mu\text{A}$ . However, when they increase the electron flux to  $1 \mu\text{A}$  for irradiating  $\text{C}_n\text{H}_{2n+2}$  ( $n=1-6$ ) and  $\text{NH}_3$  ice mixtures, they observed a one-step reaction mechanism [2].

### 3.3 The Concentration Effects in $\text{CN}^-$ -formation and the relation with $\text{C}_2\text{H}_6$ and $\text{C}_3\text{H}_8$

#### 3.3.1 Cyanide ion and Ethane

From table 3.5, we may observe that the rate  $k_1$  is nearly proportional to the concentration of  $\text{CH}_4$ . As  $\text{CH}_4$  to  $\text{NH}_3$  ratio increases in



Table 3.5: The fitting results of  $\text{CN}^-$  by equation 2.10

VUV experiments with $\text{CH}_4:\text{NH}_3$ ice mixtures			
Ratio	A ( $\times 10^{16}$ molecules $\text{cm}^{-2}$ )	$k_1$ ( $\times 10^{-18}$ photon $^{-1}$ )	$k_2$ (photon $^{-1}$ )
1:20	$4.75 \pm 0.40$	$0.70 \pm 0.09$	$>1$
1:10	$4.51 \pm 0.18$	$1.33 \pm 0.13$	$>1$
1:5	$4.61 \pm 0.18$	$1.93 \pm 0.19$	$>1$
3:2	$2.24 \pm 0.03$	$8.21 \pm 0.70$	$>1$
Quotated from Kim and Kaiser[2]			
Ratio	$[\text{CN}^-](\times 10^{16}$ molecules $\text{cm}^{-2}$ )	$k_1$ ( $\times 10^{-3}$ s $^{-1}$ )	$k_2$ ( $\times 10^{-3}$ s $^{-1}$ )
0.1 $\mu\text{A}$ e $^-$ with $\text{CH}_4:\text{NH}_3$ ice mixtures			
3:1	$1.3 \pm 0.0$	$2.7 \pm 0.3$	$8.9 \pm 1.6$
1 $\mu\text{A}$ e $^-$ with $\text{C}_n\text{H}_{2n+2}$ (n=1-6)+ $\text{NH}_3$ ice mixtures			
2:5	$1.0 \pm 0.0$	$8.7 \pm 1.3$	$\gg 1$

The second column represents the column density of  $\text{CN}^-$  we may obtain when irradiated the ice for infinitely long.

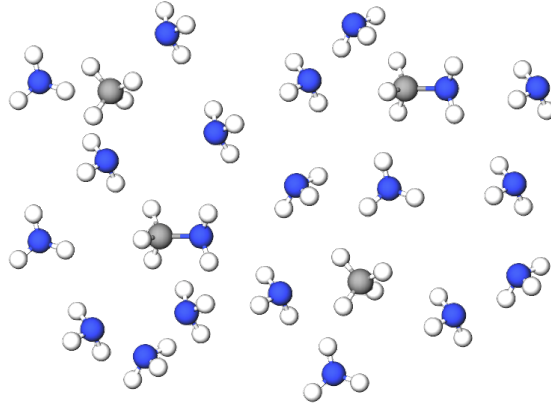


Figure 3.8: The  $\text{NH}_3$  in excess situation where increasing  $\text{CH}_4$  concentrations enhances the production of  $\text{CN}^-$ . The blue balls indicates N atoms, white balls indicates H atoms while grey ball is C atom.

ammonia dominated ices, more  $\text{CH}_4$  are involved in  $\text{CH}_3$  radical formation, thus there are more  $\text{CH}_3$  radicals to produce  $\text{CH}_3\text{NH}_2$  intermediates (figure 3.8).

In  $\text{CH}_4$  to  $\text{NH}_3 = 3:2$  ice mixtures, however, the cyanide ion formed is about half of that of the other ratios. The decrease is mainly because  $\text{NH}_2$  (forming  $\text{CH}_3\text{NH}_2$ ) has a competing relationship with  $\text{CH}_2$ ,  $\text{CH}_3$  and  $\text{C}_2\text{H}_4$  radicals (forming  $\text{C}_2\text{H}_6$  and  $\text{C}_3\text{H}_8$ ). This competition suppresses the production of intermediate  $\text{CH}_3\text{NH}_2$ , thus the formation of  $\text{CN}^-$  (figure 3.9). Therefore, the yield of  $\text{CN}^-$  is the least in  $\text{CH}_4$  to  $\text{NH}_3$  ice mixture with ratio 3:2 while the yield of  $\text{C}_2\text{H}_6$  is the greatest in the mixture with the same ratio (table 3.5 and 3.3). Figure of  $\text{CN}^-$  and  $\text{C}_2\text{H}_6$  (figure 3.10) shows the formation of  $\text{CN}^-$  in ice mixtures with di-

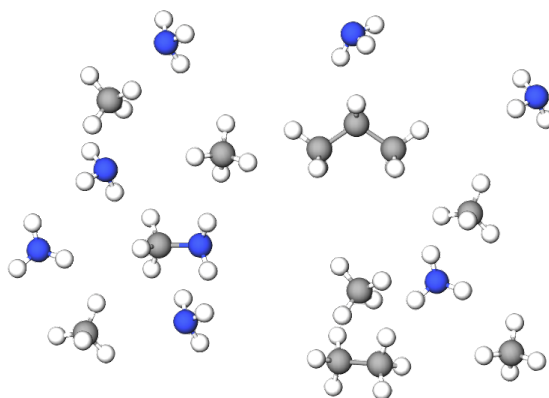


Figure 3.9: The  $\text{CH}_4$  in excess situation where  $\text{CH}_4$  reacts with neighbouring  $\text{CH}_4$  molecules producing  $\text{C}_2\text{H}_6$  and  $\text{C}_3\text{H}_8$ . The blue balls indicates N atoms, white balls indicates H atoms while grey balls are C atoms.

luted  $\text{CH}_4$  has more  $\text{CN}^-$  formed than  $\text{C}_2\text{H}_6$ . It is because ice mixtures with higher concentrations in  $\text{CH}_4$  is more effective for one  $\text{CH}_3$  radical to combine with another  $\text{CH}_3$  radical. In contrast,  $\text{CH}_3$  radicals formed in the ice mixtures with diluted  $\text{CH}_4$  concentrations are aggregated by  $\text{NH}_3$ . Therefore,  $\text{CN}^-$  is more efficient to form in ice mixtures with excess  $\text{NH}_3$ .

### 3.4 Photon Energy Effect - EUV and VUV

According to Blanksby and Ellison (2003), the dissociation energy for  $\text{CH}_4$ , becoming  $\text{CH}_3$ ,  $\text{CH}_2$ ,  $\text{CH}$  and  $\text{C}$  are 4.55, 4.79, 4.39 and 3.51 eV respectively at 298 K; whereas dissociation energy for  $\text{NH}_3$ , becoming  $\text{NH}_2$  is 4.67 eV at 298 K[25].

Considering our MDHL with average energy of 9.27 eV, all of the above fragments may exist either in the form of radicals or combine with other radicals to form heavier molecules in our ice mixtures. Although increasing the photon energy does not create new fragmentation pathway, the choice of fragmentation pathways depends on photon energy.

Several gaseous state measurements also support this statement. First, Gans et al. (2011) [26] changed VUV photon wavelengths from 121.6 nm (10.2 eV) to 118.2 nm (10.4 eV) to dissociate the  $\text{CH}_4$  molecules

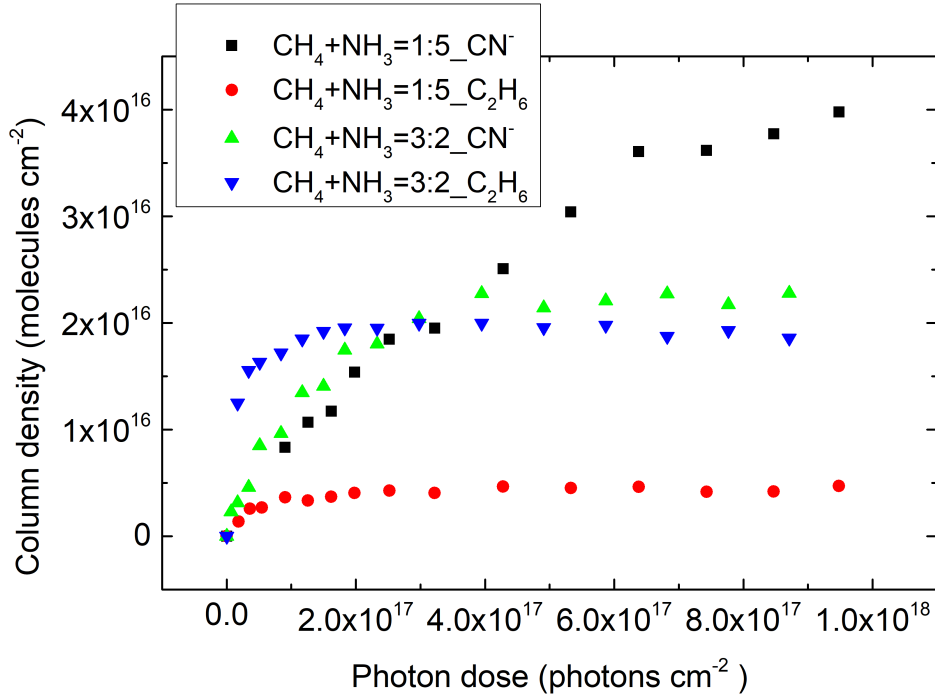


Figure 3.10: The column density of  $\text{CN}^-$  and  $\text{C}_2\text{H}_6$  accumulated when different relative proportions of  $\text{CH}_4 + \text{NH}_3$  ice mixtures are irradiated by VUV photons provided by MDHL.

and ionize the fragments with the corresponding photon energy. Changing the output of the pulsed laser from 121.6 to 118.1 nm significantly changed the ratio of  $\text{CH}_3^+$  and  $\text{CH}_2^+$ , produced from fragmentation, from 1: 1 to 1:2. This slight change of photon energy, from 10.2 eV to 10.4 eV has a significant change in the ratio between different pathways.

Second, an EUV fragmentation experiment done by Tsai et al. [27] used 30.4 nm to photo-dissociate  $\text{CH}_4$  and tested it by time-of-flight mass spectrometer yields  $\text{CH}_3^+ : \text{CH}_2^+ : \text{CH}^+ : \text{C}^+ = 1 : 0.32 : 0.118 : 0.0237$  (Tsai 1980). Consider the ratios of  $\text{CH}_3$  to  $\text{CH}_2$  radicals, it is around 3 to 1, which is in contrast to the experiment results of Gans et al. (2011)[26]. Although both of them are gaseous state experimental results, it is uncertain whether increasing photon energy can produce more  $\text{CH}_2$  radicals in ice mixtures.

Thirdly, a group varies ratios of  $\text{CH}_4 + \text{NH}_3$  mixtures and irradiate with far UV irradiation at 134 nm [28]. However, this group only used



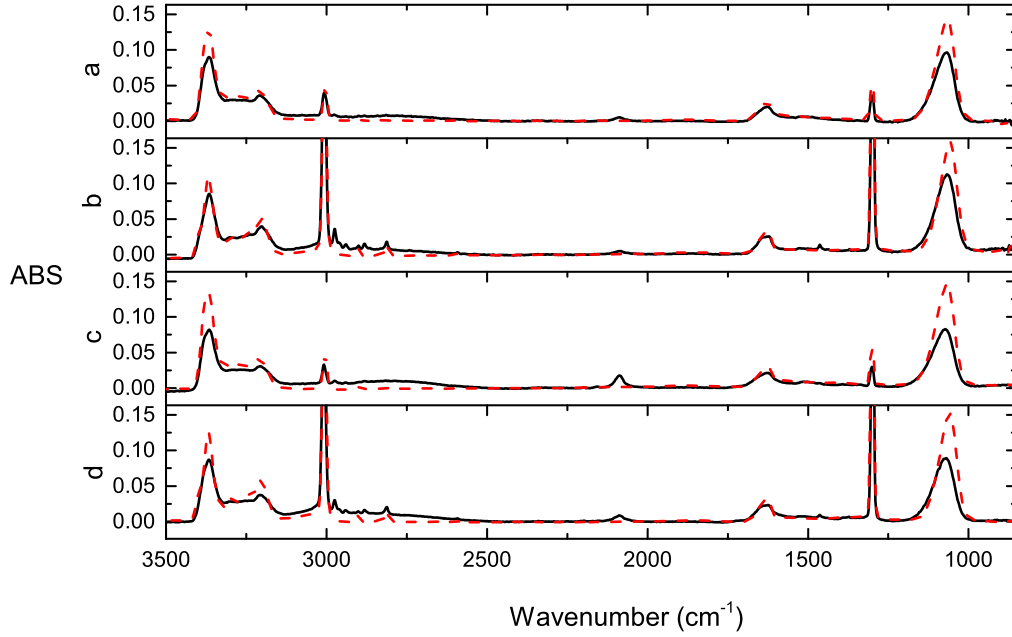


Figure 3.11: The the infrared spectrum of  $\text{CH}_4 + \text{NH}_3$  ice mixtures before irradiation (black) and VUV and EUV (coloured) irradiated ice mixtures provided by MDHL. (a) and (b) are EUV irradiated  $\text{CH}_4:\text{NH}_3 = 1:5$  and  $3:2$  ice mixtures respectively, and (c) and (d) are VUV irradiated  $\text{CH}_4:\text{NH}_3 = 1:5$  and  $3:2$  ice mixtures respectively.

gas chromatography to analyse the final products and their reaction is carried in gas phase in room temperature. We aware that the VUV absorption spectra of  $\text{CH}_4$  in solid phases is different from gaseous phases [29], so the exact photo dissociation fragmentation ratios by EUV nor VUV irradiations in astronomical environments are still unknown. It is worthwhile for us to perform the experiment by EUV irradiation to see if EUV irradiation can generate any new products on the surface of Charon, or any difference in yield.

Table 3.6 shows the identified peaks of  $\text{CH}_4 + \text{NH}_3$  ice mixtures irradiated by VUV and EUV (30.4 nm) irradiated in IR spectra (figure 3.11).

From figure 3.12, we may observe that more  $\text{C}_3\text{H}_8$  relative to  $\text{C}_2\text{H}_6$  is produced by 30.4nm (40.8 eV) photons than by VUV photons. Considering the formation mechanisms of  $\text{C}_2\text{H}_6$  and  $\text{C}_3\text{H}_8$ , equation (3.2 and 3.4), when MDHL VUV irradiation is replaced by He II 30.4 nm



Table 3.6: The peak positions of identified substances after VUV and EUV irradiations in different relative proportions of ice mixtures.

Literture assignments		CH <sub>4</sub> :NH <sub>3</sub> ratio (MDHL)		CH <sub>4</sub> :NH <sub>3</sub> ratio (30.4 nm)		Ref.
Wavenumber (cm <sup>-1</sup> )	Identified IR modes	1:5 (cm <sup>-1</sup> )	3:2 (cm <sup>-1</sup> )	1:5 (cm <sup>-1</sup> )	3:2 (cm <sup>-1</sup> )	
3375	$\nu_3$ (NH <sub>3</sub> )	3366	3367	3368	3368	1
3210	$\nu_1$ (NH <sub>3</sub> )	3207	3205	3209	3205	1
2972	$\nu_{10}$ (C <sub>2</sub> H <sub>6</sub> )	2975	2975	2977	2976	3
2960	C <sub>3</sub> H <sub>8</sub>	-	2960	-	2960	7
2941	$\nu_8 + \nu_1$ (C <sub>2</sub> H <sub>6</sub> )	2940	2940	-	2942	3
2904	$\nu_1$ (CH <sub>4</sub> )	2901	2901	2901	2901	5
2879	$\nu_5$ (C <sub>2</sub> H <sub>6</sub> )	2882	2882	-	2884	3
2814	$\nu_2 + \nu_4$ (CH <sub>4</sub> )	-	2815	-	2813	5
2083	$\nu$ (CN <sup>-</sup> )	2088	2088	2090	2089	2
1625	$\nu_4$ (NH <sub>3</sub> )	1625	1631	1627	1631	1
1514	$\delta$ (NH <sub>2</sub> )	1509	1511	1509	1511	6
1465-1440	deform CH <sub>2</sub> scissor	1461	1463	-	1465	3,4
1390-1370	CH <sub>3</sub> sym deform	1394	1372	-	1372	4
1298	$\nu_4$ (CH <sub>4</sub> )	1301	1299	1303	1301	2
1075	$\nu_2$ (NH <sub>3</sub> )	1073	1072	1070	1068	1
820	$\nu_{12}$ (C <sub>2</sub> H <sub>6</sub> )	-	820	-	-	3

Reference: 1. Bossa et al. (2008) [17] 2. Moore and Hudson (2003) [18] 3. Kim et al. (2010) [19] 4. Socrates et al. (2001) [20] 5. Bennet and Kaiser (2007) [21] 6. Zheng et al. (2008) [22] 7. Hudson and Moore (2004) [23]

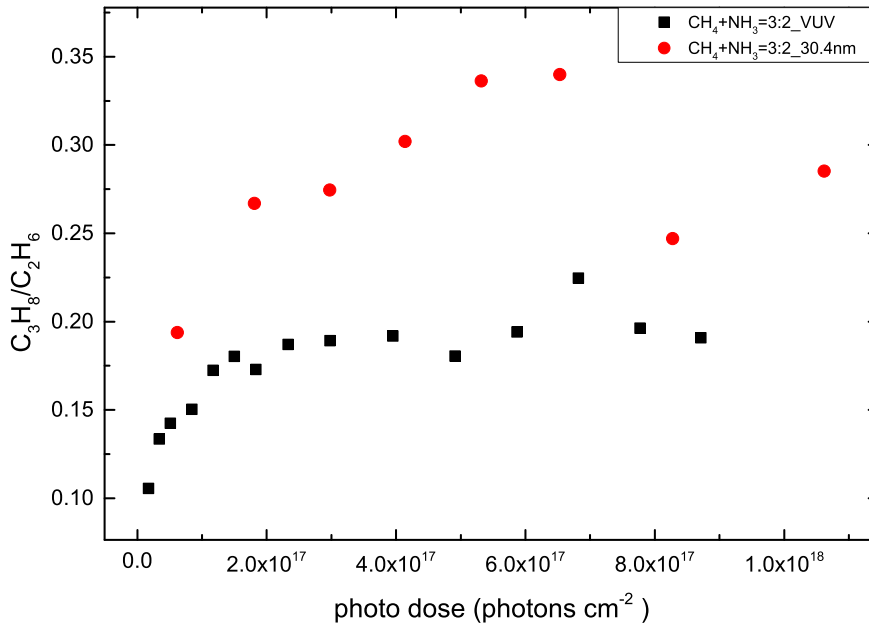


Figure 3.12: The column density of C<sub>3</sub>H<sub>8</sub> divided by C<sub>2</sub>H<sub>6</sub> accumulated when different relative proportions of CH<sub>4</sub> + NH<sub>3</sub> ice mixtures are irradiated by VUV and EUV photons

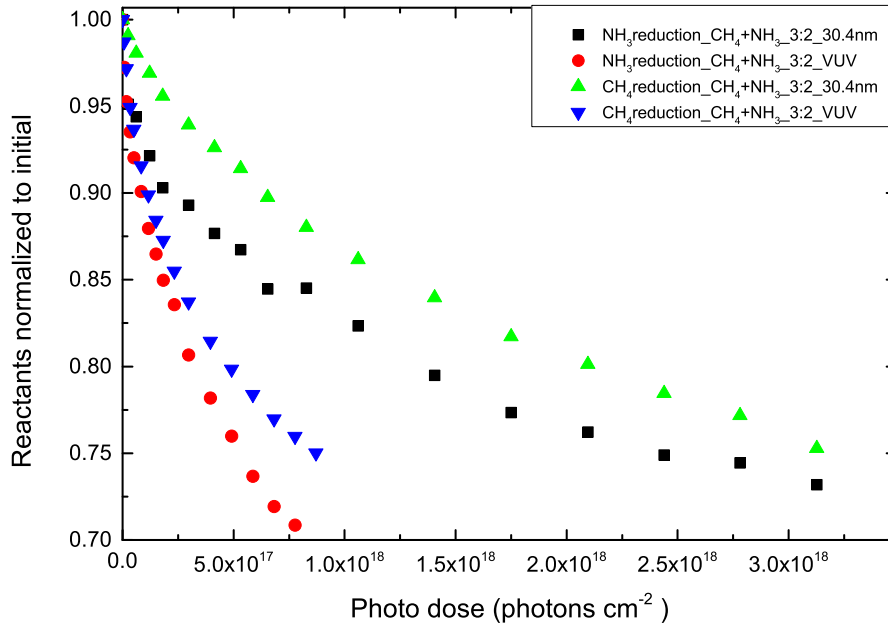


Figure 3.13: The normalized destruction of  $\text{CH}_4$  and  $\text{NH}_3$  in  $\text{CH}_4 + \text{NH}_3$  ice mixtures irradiated by VUV and EUV photons

monochromatic light, the ratio of  $\text{C}_3\text{H}_8$  to  $\text{C}_2\text{H}_6$  in  $\text{CH}_4$  to  $\text{NH}_3 = 3:2$  ice mixtures irradiated by VUV irradiation is lower than that under EUV provided by NSRRC (figure 3.12). There are many possible explanations, one of those maybe the internally excited  $\text{C}_2\text{H}_6$  can break down to be  $\text{C}_2\text{H}_4$ , which implies the production of  $\text{C}_3\text{H}_8$ . Second, it may be caused by the increase in  $\text{CH}_2$  radicals during fragmentation of  $\text{CH}_4$ , from the findings of Gans et al. (2011)[26], the ratio of  $\text{CH}_2$  radicals increases from 0.3 to 0.48 when photon energy increases from 121.6 nm to 118.2 nm in their pulsed laser experiments. Note that it is different from Tsai et al. (1980)[27].

Apart from  $\text{C}_2\text{H}_6$  and  $\text{C}_3\text{H}_8$ ,  $\text{CN}^-$  production may differ. Figure 3.14 shows the accumulated column densities of  $\text{CN}^-$  generated by irradiation of  $\text{CH}_4 + \text{NH}_3$  ice mixtures by MDHL and 30.4 nm monochromatic light. The fitting results are shown in Table 3.6. The rate constants forming  $\text{CN}^-$  is 3.06 to 4.13 times larger in  $\text{CH}_4:\text{NH}_3 = 1:5$  and  $3:2$  irradiated by MDHL than irradiated by 30.4 nm monochromatic light

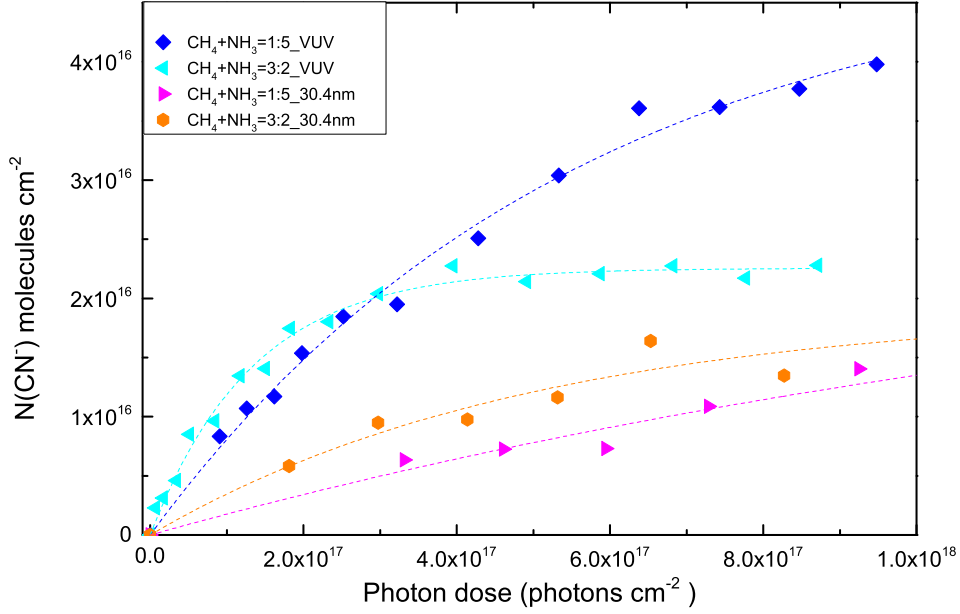


Figure 3.14: The column densities of  $\text{CN}^-$  generated by irradiation of  $\text{CH}_4+\text{NH}_3$  ice mixtures by MDHL and 30.4 nm monochromatic light.

respectively. From figure 3.13, the destruction cross-section of  $\text{CH}_4$  and  $\text{NH}_3$  are reduced by  $6.06 \pm 0.07$  and  $3.19 \pm 0.12$  times respectively. The formation rate constants of  $\text{CN}^-$  is 3.06 to 4.13 times smaller than VUV irradiations (table 3.7). Therefore, we may conclude that the decrease in  $\text{CN}^-$  formation rate by 30.4nm (40.8 eV) EUV irradiation is mainly due to the decreased  $\text{NH}_3$  destruction cross-sections. In general, the energy of MDHL has already exceeded the energy required to form the  $\text{CH}_3$  and  $\text{NH}_2$  radicals, further increasing photon energy would not pose dramatical change to  $\text{CH}_4$  and  $\text{NH}_3$  ice mixtures.

Table 3.7: The fitting results of  $\text{CN}^-$  by equation 2.10

Light source	Ratio of $\text{CH}_4:\text{NH}_3$	A ( $\times 10^{16}$ molecules $\text{cm}^{-2}$ )	$k_1$ ( $\times 10^{-18}$ photon $^{-1}$ )	$k_2$ (photon $^{-1}$ )
VUV	1:5	$4.61 \pm 0.18$	$1.93 \pm 0.19$	>1
MDHL	3:2	$2.24 \pm 0.03$	$8.21 \pm 0.70$	>1
EUV	1:5	$2.89 \pm 1.29$	$0.63 \pm 0.37$	>1
30.4nm	3:2	$2.24 \pm 0.03$	$1.92 \pm 1.99$	>1

Fitting result of figure 3.14 with pseudo first order equation  $[\text{CN}^-] = A(1 - e^{-kx})$ . These fitting results of MDHL experiments are an average of at least 2 experiments with the same circumstances. In the expression, A represents the column density when x, the photon dose, becomes infinitely large and k is the rate constant.



### 3.5 Residues

The residues we studied are the accumulated substances remained on the substrate after warmed up. Figure 3.15 is a comparison of  $\text{CH}_4:\text{NH}_3 = 3:2$  after VUV experiments, residues accumulate after EUV exposure of  $\text{CH}_4:\text{NH}_3 = 3:2$  ice mixtures and the plasma experiment done by Imanaka et al. (2004)[14]. The peak positions and assignments are listed at table 3.8. The residues formed in irradiated ammonia dominating  $\text{CH}_4+\text{NH}_3$  ice mixtures is not observed after accumulation of consecutive experiments. There are no differences between EUV accumulated residues and VUV accumulated residues in  $\text{CH}_4:\text{NH}_3 = 3:2$  ice mixtures. The main functional groups (nitrogen position) of the residues are conjugated nitriles. Based on experiments of  $\text{N}_2+\text{CH}_4$  (9:1) done at 2300 Pa. by Imanaka et al. (2004)[14], the tholins formed at high pressure (2300 Pa) should be a polymer-like branched chain structure terminated with  $-\text{CH}_3$   $-\text{NH}_2$  and  $-\text{C}\equiv\text{N}$  with few aromatic compounds.

Table 3.8: The peak positions of residues and their assignments

Imanaka et al. (2004) $\nu$ ( $\text{cm}^{-1}$ )	implied functional group	VUV (MDHL) $\nu$ ( $\text{cm}^{-1}$ )	EUV (30.4 nm) $\nu$ ( $\text{cm}^{-1}$ )
2954 - 2972	$-\text{CH}_3$ - asymmetric stretching	2955	2962
2929 - 2932	$-\text{CH}_2$ - asymmetric stretching	2923	2929
2869 - 2874	$-\text{CH}_3$ - symmetric stretching	2871	2871
2173 - 2189	conjugated nitriles, such as with $-\text{C}=\text{C}(-\text{NH}_2)$ $\text{C}-\text{N}\equiv\text{C}$ stretching	2173	2174
1460	$\text{C}-\text{CH}_3$ asymmetric bending	1451	1451
1375-1379	$\text{C}-\text{CH}_3$ umbrella symmetric bending	1372	1378

We may get similar residues by using different initial reactants (replacing  $\text{N}_2$  by  $\text{NH}_3$ ). The similarities during formation of atomic nitrogens when breaking  $\text{N}\equiv\text{N}$  bonds in nitrogen molecules ( $\text{N}_2$ ) and N-H bonds in ammonia give rise to this result. When photon energy is enough to break both NH bond and  $\text{N}\equiv\text{N}$  bond, similar experimental residues forms. Our results implies that the residues formed on Charon is similar to what they found on Titan, although their formation environments differs from gaseous phase with  $\text{N}_2$  dominating to solid phase with  $\text{NH}_3$ .

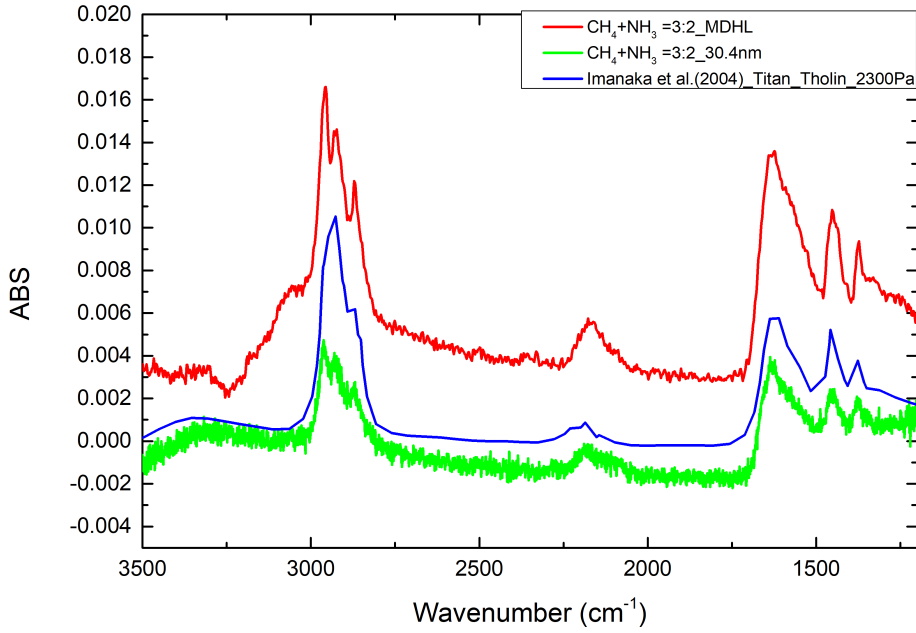


Figure 3.15: The IR spectrum of residues in after  $\text{CH}_4:\text{NH}_3 = 3:2$  experiments and the accumulate residues after MDHL experiments and NSRRC experiments.

### 3.6 Summary

The main product of VUV and EUV irradiated  $\text{CH}_4+\text{NH}_3$  ice mixtures are  $\text{C}_2\text{H}_6$  and  $\text{CN}^-$ .  $\text{C}_3\text{H}_8$  is also produced by  $\text{C}_2\text{H}_6$  or  $\text{C}_2\text{H}_2$ . We do several investigations towards  $\text{CH}_4+\text{NH}_3$  ice mixtures. First, by changing ratio of  $\text{CH}_4$  to  $\text{NH}_3$  ice mixtures,  $\text{CN}^-$  production is more effective in  $\text{NH}_3$  dominated ice mixtures. While in contrast,  $\text{C}_2\text{H}_6$  is the main product when  $\text{CH}_4$  dominates. Second, by changing the photon source to EUV irradiation, the yield of  $\text{C}_3\text{H}_8$  increases. By studying the production efficiencies, the difference in photo-production yield is mainly caused by the decrease in photo-destruction cross-section in the reactants. Finally, we compare our residues obtained with laboratory produced Taitan tholins, the similar infrared spectrum shows a similar functional groups in residues. Our result implies that the tholin on Charon should be similar to that of Titan.



## 4. Astrophysical Implications

The main source to irradiating the dark side of Charon is  $\text{Ly}\alpha$ , reflected by interplanetary medium [4]. Other sources include energetic ions in solar wind, which mainly consist of  $\text{H}^+$ ,  $\text{He}^+$ ,  $\text{He}^{++}$  and  $\text{O}^{2+}$ , etc. originated from solar corona or IPM. Helium ion emits He II line in all directions when they falls back to the ground state including the dark side of Charon. He II irradiation as it is 3 to 20 times more intense than He I during a solar flare. As the intensity varies with solar activities, it is difficult to estimate the dose onto Charon.

In this chapter, we will discuss the impacts of three difference energy sources , including EUV, VUV and energetic (5 keV) electrons on production of cyanide ions and their implication on Charon. First, we compare the destructive cross-sections of these sources, and then their corresponding production yields in  $\text{CN}^-$ .

### 4.1 The destruction of methane and ammonia by photon sources and electrons

In electron irradiation experiments of Kim and Kaiser (2011)[2], the energy transferred to  $\text{CH}_4 + \text{NH}_3$  ice mixtures is by linear electron transfer (LET) of  $3.1 \text{ keV } \mu\text{m}^{-1}$ , in the order of magnitude of the MeV cosmic rays typically transferred to the ice samples. Their dose reached  $1.3 \text{ eV molecule}^{-1}$  in 90 minutes with about 610 ML of  $\text{CH}_4$  and 260 ML of  $\text{NH}_3$ .

The percentage of photons absorbed by  $\text{CH}_4$  and  $\text{NH}_3$  ice mixtures under VUV irradiation is calculated by substituting cross-sections measured by Cruz-Diaz et al. (2014) [29] and the VUV intensity spectrum of our MDHL into Beer's law.  $\text{CH}_4:\text{NH}_3 = 3:2$  ice mixtures can absorb more than 99 % of light when thickness of  $\text{NH}_3$  equals 600 ML (figure 4.1). Therefore, we may assume all the irradiated light is absorbed by

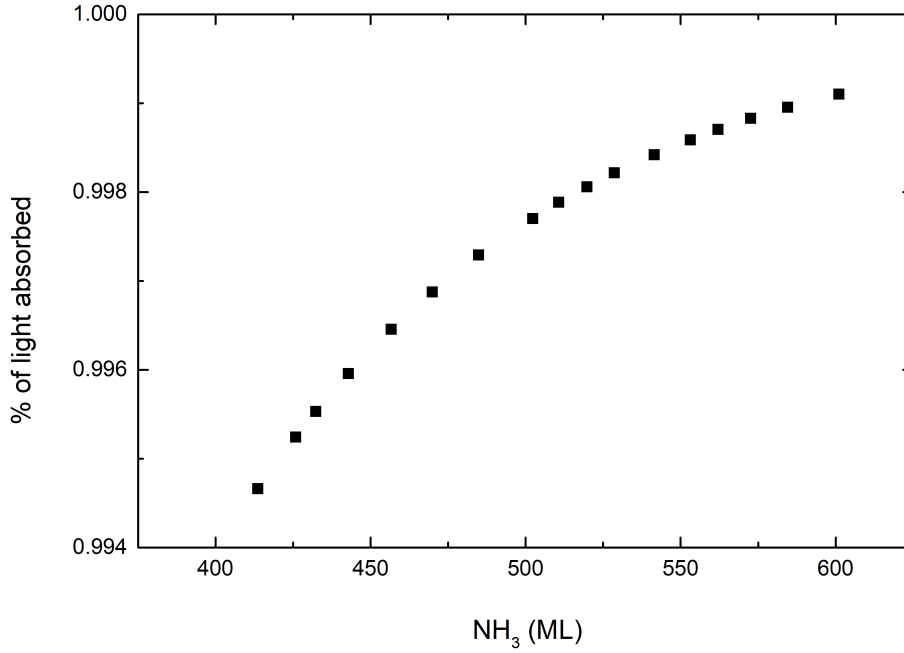


Figure 4.1: The calculated percentage of VUV irradiation absorbed by different thickness of CH<sub>4</sub> to NH<sub>3</sub> = 3:2 ice mixtures.

the ice. For CH<sub>4</sub>:NH<sub>3</sub> = 3:2 ice mixture, around  $9 \times 10^{17}$  photons are irradiated in 270 minutes.

Regarding EUV irradiations, since there are no suitable windows (used for cutting off higher order lights) to measure the absorption of ices, it is impossible to obtain absorption cross-sections right now. From figure 3.13, we obtain the destructive cross-sections of EUV to VUV photons. The CH<sub>4</sub> destruction by EUV photons is  $6.06 \pm 0.07$  times lower than VUV irradiation. From the New Horizons Mission, EUV irradiation ( $>12.4$  eV) is  $8.7 \times 10^7 \text{ eV cm}^{-2} \text{ s}^{-1}$  at mean heliocentric distance (39 A.U.) of Charon whereas VUV irradiation (Ly- $\alpha$  photons) is  $1.9 \times 10^9 \text{ eV cm}^{-2} \text{ s}^{-1}$  [4]. Since VUV flux is one order of magnitude more intense than EUV fluxes and the CH<sub>4</sub> destruction is about 6 times higher than EUV irradiation, it is the main source causing the destruction of CH<sub>4</sub>.

## 4.2 Cyanide ion produced by photon sources and electrons

Considering the ice mixtures in which CH<sub>4</sub> is dominated, the efficiencies in CN<sup>-</sup> formation by electrons and VUV irradiations is calcu-





lated by the final column densities divided by the column densities of the limiting reactant. A fixed amount of  $\text{CN}^-$  is obtained after irradiations. In our MDHL experiments, we have 14.8 ML of  $\text{CN}^-$  obtained in ( $\text{CH}_4 = 900 \text{ ML}$ ,  $\text{NH}_3 = 600 \text{ ML}$ ) ice mixtures. Kim and Kaiser (2011) irradiated ice mixtures ( $\text{CH}_4 = 610 \text{ ML}$ ,  $\text{NH}_3 = 260 \text{ ML}$ ) and obtained 13 - 16 ML of  $\text{CN}^-$  adopting the  $\text{CN}^-$  absorption coefficient ( $3.7 \times 10^{-18} \text{ cm molecule}^{-1}$ ) [30], which is 4.86 times smaller than the absorption strength adopted. We do not adopt the same absorption coefficient because the absorption strength is based on gas phase experiments and models. We adopted the absorption strength calculated by Noble et al. (2012) [16] based on experiments mixing  $\text{CH}_4$  and  $\text{NH}_3$  in room temperatures and deposited at 20 K. If they adopt the same absorption coefficient, the production yield of  $\text{CN}^-$  should be divided by 4.86. Therefore, regarding percentage of  $\text{NH}_3$  (limiting reactant), Kim and Kaiser has 1 % yield where we have 2.47 % yield in relative proportion of  $\text{CH}_4:\text{NH}_3 = 3:2$ .

The depositing (hitting) rates of  $\text{CH}_4$  onto the surface of Charon, shown in figure ??, varies from 2 to  $6 \times 10^{11} \text{ m}^{-2} \text{ s}^{-1}$  due to the tidal locked rotation of Pluto and Charon. In 1 Pluto winter (130 earth years), around 82 ML of  $\text{CH}_4$  will be deposited onto the poles, and 3 times more abundant than that at the poles facing Pluto. Since Charon-Pluto is a tidal locked relation, it is reasonable to predict that one of the surface is with more  $\text{CH}_4$  hitting rates and hence condenses more  $\text{CH}_4$ .

The experimental situation is ideal to apply on very thick ices, where photons or electrons can irradiate the surface without renewal since (covered by non-irradiated  $\text{CH}_4$  ice) we have nearly 100 percent absorption in VUV photons (figure 4.1). Our experimental results can be applied to calculate the surface column densities of  $\text{CN}^-$  and  $\text{C}_2\text{H}_6$  on Charon after the winter times. The ice would be further processed by EUV or other energetic energy sources when directly facing to the sun. Therefore, information of pre-irradiated ices during winter times is helpful to future studies, of which compositions are known for irradiation experiments by other energetic sources like electrons.



From our experiments, irradiation of  $7.6 \times 10^{17}$  VUV photons is the irradiations irradiated on Charon in about 0.5 Pluto year. As a result, under winter time, if we only consider VUV photon source, assuming ratio of  $\text{CH}_4$  to  $\text{NH}_3$  is 3:2, 1:5, 1:10 and 1:20, about 22.5, 36.6, 29.5 and 18.9 ML of  $\text{CN}^-$  will be formed during winter time respectively (figure 3.14).

### 4.3 Conclusion

Through investigating methane( $\text{CH}_4$ ) and ammonia( $\text{NH}_3$ ) ice mixtures, we better understand the followings relations: 1. The formation yield of cyanide ion ( $\text{CN}^-$ ) is not proportional to the initial deposited methane when methane is dominating. However, the formation rate is proportional to its initial  $\text{CH}_4$  to  $\text{NH}_3$  ratios. The competition between  $\text{CH}_3$  radicals (forming both  $\text{CH}_3\text{NH}_2$  and  $\text{C}_2\text{H}_6$ ) and  $\text{NH}_2$  radicals (forming  $\text{CH}_3\text{NH}_2$ ) results in the former result. 2. When VUV is replaced by 40.8 eV 30.4nm (40.8 eV) He II EUV irradiations, the destruction cross-section of  $\text{CH}_4$  and  $\text{NH}_3$  are reduced by  $6.06 \pm 0.07$  and  $3.19 \pm 0.12$  times respectively. The lower formation rate of  $\text{CN}^-$  in EUV irradiation by 3.06 to 4.13 times is mainly due to the reduced  $\text{NH}_3$  destruction cross-sections. 3. The functional groups of residues obtained in  $\text{CH}_4$  to  $\text{NH}_3 = 3:2$  ice mixtures are similar to the laboratory made Titan tholins. 4. The formation of  $\text{CN}^-$  with different ratios of  $\text{CH}_4$  to  $\text{NH}_3$  ice mixtures provides valuable informations on the surface compositions of Charon after winter time.



## Bibliography

- [1] S. Miyakawa, H. J. Cleaves, and S. L. Miller, “The cold origin of life: B. implications based on pyrimidines and purines produced from frozen ammonium cyanide solutions,” *Origins of Life and Evolution of Biospheres*, vol. 32, no. 3, pp. 209–218, 2002.
- [2] Y. Kim and R. Kaiser, “on the formation of amines ( $\text{RNH}_2$ ) and the cyanide anion ( $\text{CN}^-$ ) in electron-irradiated ammonia-hydrocarbon interstellar model ices,” *The Astrophysical Journal*, vol. 729, no. 1, p. 68, 2011.
- [3] W. Grundy, R. Binzel, B. Buratti, J. Cook, D. Cruikshank, C. Dalle Ore, A. Earle, K. Ennico, C. Howett, A. Lunsford *et al.*, “Surface compositions across Pluto and Charon,” *Science*, vol. 351, no. 6279, p. aad9189, 2016.
- [4] W. Grundy, D. Cruikshank, G. Gladstone, C. Howett, T. Lauer, J. Spencer, M. Summers, M. Buie, A. Earle, K. Ennico *et al.*, “The formation of Charon’s red poles from seasonally cold-trapped volatiles,” *Nature*, vol. 539, no. 7627, pp. 65–68, 2016.
- [5] Y.-J. Chen, K.-J. Chuang, G. M. Caro, M. Nuevo, C.-C. Chu, T.-S. Yih, W.-H. Ip, and C.-Y. Wu, “Vacuum ultraviolet emission spectrum measurement of a microwave-discharge hydrogen-flow lamp in several configurations: application to photodesorption of CO ice,” *The Astrophysical Journal*, vol. 781, no. 1, p. 15, 2013.
- [6] L. d’Hendecourt and L. Allamandola, “Time dependent chemistry in dense molecular clouds. iii-infrared band cross sections of molecules in the solid state at 10 K,” *Astronomy and Astrophysics Supplement Series*, vol. 64, pp. 453–467, 1986.



- [7] J. C. Cook, S. J. Desch, T. L. Roush, C. A. Trujillo, and T. Geballe, “Near-infrared spectroscopy of Charon: Possible evidence for cryo-volcanism on Kuiper belt objects,” *The Astrophysical Journal*, vol. 663, no. 2, p. 1406, 2007.
- [8] M. E. Brown and W. M. Calvin, “Evidence for crystalline water and ammonia ices on Pluto’s satellite Charon,” *Science*, vol. 287, no. 5450, pp. 107–109, 2000.
- [9] W. A. Hoey, S. K. Yeoh, L. M. Trafton, D. B. Goldstein, and P. L. Varghese, “Rarefied gas dynamic simulation of transfer and escape in the Pluto–Charon system,” *Icarus*, no. 287, pp. 87–102, 2017.
- [10] G. R. Gladstone, W. R. Pryor, and S. A. Stern, “Ly $\alpha$ @ pluto,” *Icarus*, vol. 246, pp. 279–284, 2015.
- [11] S. Kundu, V. S. Prabhudesai, and E. Krishnakumar, “Electron induced reactions in condensed mixtures of methane and ammonia,” *Physical Chemistry Chemical Physics*, vol. 19, no. 37, pp. 25 723–25 733, 2017.
- [12] S. Stern, J. Kammer, G. Gladstone, A. Steffl, A. Cheng, L. Young, H. Weaver, C. Olkin, K. Ennico, J. W. Parker *et al.*, “New horizons constraints on charon’s present day atmosphere,” *Icarus*, vol. 287, pp. 124–130, 2017.
- [13] T.-F. Hsieh, L.-R. Huang, S.-C. Chung, T.-E. Dann, P.-C. Tseng, C. Chen, and K.-L. Tsang, “Design of a high-flux and high-resolution VUV bending-magnet beamline,” *Journal of synchrotron radiation*, vol. 5, no. 3, pp. 562–564, 1998.
- [14] H. Imanaka, B. N. Khare, J. E. Elsila, E. L. Bakes, C. P. McKay, D. P. Cruikshank, S. Sugita, T. Matsui, and R. N. Zare, “Laboratory experiments of titan tholin formed in cold plasma at various pressures: implications for nitrogen-containing polycyclic aromatic compounds in titan haze,” *Icarus*, vol. 168, no. 2, pp. 344–366, 2004.
- [15] M. Moore and R. Hudson, “Infrared study of ion-irradiated water-ice mixtures with hydrocarbons relevant to comets,” *Icarus*, vol. 135, no. 2, pp. 518–527, 1998.



- [16] J. A. Noble, P. Theule, F. Borget, G. Danger, M. Chomat, F. Duvernay, F. Mispelaer, and T. Chiavassa, “The thermal reactivity of HCN and NH<sub>3</sub> in interstellar ice analogues,” *Monthly Notices of the Royal Astronomical Society*, vol. 428, no. 4, pp. 3262–3273, 2012.
- [17] J.-B. Bossa, P. Theulé, F. Duvernay, F. Borget, and T. Chiavassa, “Carbamic acid and carbamate formation in NH<sub>3</sub>+CO<sub>2</sub> ices–UV irradiation versus thermal processes,” *Astronomy & Astrophysics*, vol. 492, no. 3, pp. 719–724, 2008.
- [18] M. Moore and R. Hudson, “Infrared study of ion-irradiated N<sub>2</sub>-dominated ices relevant to Triton and Pluto: Formation of HCN and HNC,” *Icarus*, vol. 161, no. 2, pp. 486–500, 2003.
- [19] Y. Kim and R. Kaiser, “Abiotic formation of carboxylic acids (RCOOH) in interstellar and solar system model ices,” *The Astrophysical Journal*, vol. 725, no. 1, p. 1002, 2010.
- [20] G. Socrates, “Infrared and raman characteristic group frequencies, 3rd,” 2001.
- [21] C. J. Bennett and R. I. Kaiser, “The formation of acetic acid (CH<sub>3</sub>COOH) in interstellar ice analogs,” *The Astrophysical Journal*, vol. 660, no. 2, p. 1289, 2007.
- [22] W. Zheng, D. Jewitt, Y. Osamura, and R. I. Kaiser, “Formation of nitrogen and hydrogen-bearing molecules in solid ammonia and implications for solar system and interstellar ices,” *The Astrophysical Journal*, vol. 674, no. 2, p. 1242, 2008.
- [23] R. Hudson and M. Moore, “Reactions of nitriles in ices relevant to Titan, comets, and the interstellar medium: formation of cyanate ion, ketenimines, and isonitriles,” *Icarus*, vol. 172, no. 2, pp. 466–478, 2004.
- [24] C. J. Bennett, C. S. Jamieson, Y. Osamura, and R. I. Kaiser, “Laboratory studies on the irradiation of methane in interstellar, cometary, and solar system ices,” *The Astrophysical Journal*, vol. 653, no. 1, p. 792, 2006.



- [25] S. J. Blanksby and G. B. Ellison, “Bond dissociation energies of organic molecules,” *Accounts of chemical research*, vol. 36, no. 4, pp. 255–263, 2003.
- [26] B. Gans, S. Boyé-Péronne, M. Broquier, M. Delsaut, S. Douin, C. E. Fellows, P. Halvick, J.-C. Loison, R. R. Lucchese, and D. Gauyacq, “Photolysis of methane revisited at 121.6 nm and at 118.2 nm: quantum yields of the primary products, measured by mass spectrometry,” *Physical Chemistry Chemical Physics*, vol. 13, no. 18, pp. 8140–8152, 2011.
- [27] B. P. Tsai and J. H. Eland, “Mass spectra and doubly charged ions in photoionization at 30.4 nm and 58.4 nm,” *International Journal of Mass Spectrometry and Ion Physics*, vol. 36, no. 2, pp. 143–165, 1980.
- [28] A. Bossard and G. Toupance, “Far UV photolysis of CH<sub>4</sub>-NH<sub>3</sub> mixtures and planetary studies,” *Nature*, vol. 288, no. 5788, pp. 243–246, 1980.
- [29] G. Cruz-Diaz, G. M. Caro, Y.-J. Chen, and T.-S. Yih, “Vacuum-UV spectroscopy of interstellar ice analogs-I. Absorption cross-sections of polar-ice molecules,” *Astronomy & Astrophysics*, vol. 562, p. A119, 2014.
- [30] M. K. Georgieva and E. A. Velcheva, “Computational and experimental studies on the ir spectra and structure of the simplest nitriles (C1 and C2), their anions, and radicals,” *International journal of quantum chemistry*, vol. 106, no. 6, pp. 1316–1322, 2006.